

# The Importance of Architecture Choice in Deep Learning for Climate Applications

Simon Dräger<sup>1</sup> Maike Sonnewald<sup>1</sup>

## Abstract

Machine Learning has become a pervasive tool in climate science applications. However, current models fail to address nonstationarity induced by anthropogenic alterations in greenhouse emissions and do not routinely quantify the uncertainty of proposed projections. In this paper, we model the Atlantic Meridional Overturning Circulation (AMOC) which is of major importance to climate in Europe and the US East Coast by transporting warm water to these regions, and has the potential for abrupt collapse. We can generate arbitrarily extreme climate scenarios through arbitrary time scales which we then predict using neural networks. Our analysis shows that the AMOC is predictable using neural networks under a diverse set of climate scenarios. Further experiments reveal that MLPs and Deep Ensembles can learn the physics of the AMOC instead of imitating its progression through autocorrelation. With quantified uncertainty, an intriguing pattern of “spikes” before critical points of collapse in the AMOC casts doubt on previous analyses that predicted an AMOC collapse within this century. Our results show that Bayesian Neural Networks perform poorly compared to more dense architectures and care should be taken when applying neural networks to nonstationary scenarios such as climate projections. Further, our results highlight that big NN models might have difficulty in modeling global Earth System dynamics accurately and be successfully applied in nonstationary climate scenarios due to the physics being challenging for neural networks to capture.

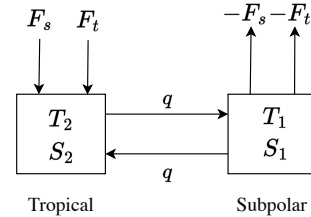


Figure 1. Stommel box model with a fresh water forcing and a temperature forcing. Note that this is the “extended variant” where we obtain the standard variant by setting  $F_t \equiv 0$ .

## 1. Introduction

Climate change has a significant impact on our planet and society, with many unknown variables. One of these variables is the Atlantic Meridional Overturning Circulation (AMOC) which transports warm water from the tropics to the US East Coast and Europe. Without the AMOC, these places would be uninhabitable due to ice age conditions, however, recent climate developments induce significant nonstationarity into the AMOC system with largely uncertain outcomes. An interesting part of the AMOC is its *tipping point behavior* (Tziperman, 2022; Lenton et al., 2008). A tipping point (Lenton et al., 2008; Van Nes et al., 2016) is defined as a point in a system which upon a small perturbation leads to a dramatic change within the system. This tipping point behavior is especially interesting due to anthropogenic climate change driving the AMOC in the aforementioned *nonstationary* way, ultimately leading toward a tipping point (Tziperman, 2022). By nonstationary, we mean for example a non-constant amplitude of sinusoidal green house emissions (stationary, on the other hand, would mean the emissions have the same mean and standard deviation over time). To deal with the challenge of increasingly nonstationary AMOC (and climate, by extension) behavior, we wish to take advantage of the predictive abilities that Machine Learning (ML) methods provide. Here, we present new insight into the extent that different neural network architectures are able to learn the AMOC’s physics, how they work in nonstationary climate scenarios and how uncertain their predictions are.

With the inception of ML as a pervasive tool for predic-

<sup>1</sup>Department of Computer Science, University of California, Davis, USA. Correspondence to: Simon Dräger <sdraeger@ucdavis.edu>.

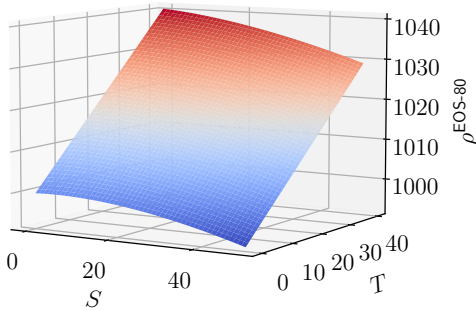


Figure 2.  $\rho^{\text{EOS-80}}(T, S)$  plotted on  $T \times S \subset [0, 40]^2$ .  $\rho^{\text{EOS-80}}(T, S)$  is concave, and thus nonlinear, in  $S$ .

tive modeling, different questions of societal importance, including climate science and oceanography (see for example (Sonnewald et al., 2021; Jones, 2017; Irrgang et al., 2021)), have been addressed. We identify three key open questions that remain unaddressed: *Firstly*, it remains unknown how well ML methods such as neural networks are able to capture the underlying system behavior of the climate system. In order to use neural networks confidently we need to know what determines a trained network’s ability to estimate out-of-sample climate data reliably and whether its skill corresponds to the underlying physics. If a net performs well only due to spurious correlations in the input data, using the net for inference could lead to devastating societal impact from wrong inference. *Secondly*, it is unclear how confidently a neural net can be used with the nonstationary forcing imposed by anthropogenically induced greenhouse gases. As such, we are projecting systems, such as the AMOC, with known instabilities into an unknown future by asking neural nets to be skillful out-of-sample, like predicting a “tipping point” they previously have never seen. *Thirdly*, there is no doubt that any prediction, physics- or ML-based, will have some nonzero uncertainty associated with it. Thus, it is imperative to be able to quantify the uncertainty of a neural net’s prediction for it to be socially useful.

The question of whether a neural net has “learned” physics and if it can be applied out-of-sample with low or quantified uncertainty are fascinating problems within the field of ML. Here we illustrate how skillful different architectures are at predicting the AMOC, how well neural networks are able to capture the underlying physics using Explainable AI (XAI, described further below) and how confidently they perform under nonstationary conditions using an ensemble approach. In particular, we are interested in understanding the intrinsic differences between neural nets trained on physics-informed features vs. autoregressively, which established the duality *understanding vs. imitating* the AMOC system.

Due to its importance, the AMOC and its potential for a shut-

down or rapid change is studied using conventional tools within climate science, such as climate models (Menary et al., 2013; Swingedouw et al., 2013; Cheng et al., 2013; Wen et al., 2016; Jackson et al., 2023), but also using simpler statistical tools, such as stochastic process modeling using a Stochastic Differential Equation (SDE) (Ditlevsen & Ditlevsen, 2023). The projections of these statistical tools recently caused alarm, suggesting an AMOC shutdown could happen as soon as 2025 (Ditlevsen & Ditlevsen, 2023). However, such methods rely on making very strong assumptions about the AMOC system. With neural networks being universal function approximators, we are less reliant on assumptions and we see much promise for the use of Machine Learning.

The use of Machine Learning is already prevalent in weather forecasts (Pathak et al., 2022; Singh et al., 2019; Salman et al., 2015), as well as to predict and explain the impact of global heating on the North Atlantic Ocean (Sonnewald & Lguensat, 2021). More recently, research on the ocean (Bire et al., 2023) started employing the Fourier Neural Operator (FNO; (Li et al., 2020)) in a novel ocean emulator system. Previous efforts (Hazeleger et al., 2013; Matei et al., 2012; Mahajan et al., 2011) at predicting the AMOC are limited to short time scales within 10 years into the future and are unable to simulate and quantify concrete climate change variables such as greenhouse gas emissions.

Measured AMOC data is not abundant and only about 20 years of contiguous AMOC data have been collected so far (McCarthy et al., 2015). This significant drawback of using real world data to predict the AMOC is limiting accurate future projections and usually does not incorporate the driving variables of the AMOC. A different downside is that none of the previously mentioned works on ocean modeling assess the question of whether the neural network has captured the underlying physical system, or if the net is fit for deployment in nonstationary applications. In our work, we model the North Atlantic Ocean using a physical system and subsequently attempt to predict its behavior using neural networks. In addition, we not only predict but *explain* why different network architectures predicted the system in the way they did, yielding an approach that is flexible and can use any time scale (months, years, 1000s of years).

We consider a model of the Atlantic Ocean consisting of two boxes; a northern and a southern box. This model is also called the “Stommel box model” (Stommel, 1961) and is canonically used to model ocean circulation like the AMOC. In the Stommel box model, each box is assigned a variable temperature  $T_i$  and a salinity  $S_i$  where  $i \in \{1, 2\}$ . The AMOC is represented as a variable  $q$  and  $F_s$  is an external fresh water forcing originating from anthropogenic climate change. In Figure 1, we depict a schematic of the Stommel

Forcing Setup Identifier	$F_s$	$F_t$	$\rho$
$\mathcal{F}_1$	Linear	—	$\rho^{\text{lin}}$
$\mathcal{F}_2$	Stationary sinusoidal	—	
$\mathcal{F}_3$	Nonstationary sinusoidal	—	
$\mathcal{F}_4$	Linear	Linear	$\rho^{\text{EOS-80}}$
$\mathcal{F}_5$	Stationary sinusoidal	Stationary sinusoidal	
$\mathcal{F}_6$	Nonstationary sinusoidal	Nonstationary sinusoidal	

Table 1. The set of forcing setups that we consider in our experiments.

model with a fresh water and a temperature forcing, i.e., external water that flows into the southern box as well as greenhouse emissions altering its temperature. We list all parameters for the box model along with their values for this paper in Appendix A, Table 2.

At the heart of the Stommel box model lie the concepts *breakdown* and *recovery*. *Breakdown* refers to the exceeding of a point in the model that leads to a sudden collapse of the AMOC (Liu et al., 2017; Tziperman, 2022). Similarly, the inverse concept *recovery* denotes the return of the AMOC to a previous state in which it had not collapsed (Thomas & Fedorov, 2019). The Stommel box model thus gives us three stable states a neural net should be able to model and a relatively simple attractor basin that emerges through the combination of equations describing the box model. This attractor basin and its underlying equations are what the neural net should “learn”. From a neural network perspective, ensemble neural nets offer an intuitive avenue in terms of exploring the attractor basin since it is known that there exist three equally important stable states in the Stommel box model (Tziperman, 2022).

## 2. Modeling the AMOC using Physical Equations and Neural Networks

### 2.1. Importance of Density and its Approximation

The *density*  $\rho_i$  in each box of the Stommel model depends on  $T_i$  and  $S_i$  and fundamentally affects  $q$  via the difference in  $\rho_i$  between both boxes (Tziperman, 2022). There exist two ways to model the water density in box 1 and 2. The first is a linear approximation

$$\rho(T, S) = \rho_0 - \alpha(T - T_0) + \beta(S - S_0) \quad (1)$$

where  $\rho_0$  is a baseline density value and  $T_0, S_0$  are baseline values for temperature and salinity, respectively.  $\alpha$  and  $\beta$  are the thermal expansion and haline contraction coefficients. The second is the Equation of State (EOS-80; (Fofonoff, 1985)) for seawater, which for a reference pressure (in this paper, atmospheric pressure) nonlinearly approximates seawater density. Due to its size we do not outline it here.

### 2.2. Modeling $q$

**Nonlinear case.** We begin with  $\rho$  being nonlinear. First, let  $\tau$  be the time step which we use to model the evolution of  $S_i$  and  $T_i$  through time (Tziperman, 2022):

$$\frac{\partial S_1}{\partial \tau} = \frac{|q|(S_2 - S_1) - F_s(\tau)}{V_1} \quad (2)$$

$$\frac{\partial S_2}{\partial \tau} = \frac{|q|(S_1 - S_2) + F_s(\tau)}{V_2} \quad (3)$$

$$\frac{\partial T_1}{\partial \tau} = \frac{|q|(T_2 - T_1) - F_t(\tau)}{V_1} \quad (4)$$

$$\frac{\partial T_2}{\partial \tau} = \frac{|q|(T_1 - T_2) + F_t(\tau)}{V_2} \quad (5)$$

with  $V_i$  being the volume of the  $i$ -th box.  $F_s(\tau)$ , a fresh water forcing, and  $F_t(\tau)$ , a temperature forcing, represent ice melting in the polar region or increased heat due to elevated greenhouse gas levels. These allow us to effectively simulate different climate scenarios. Note that  $F_t(\tau)$  is optional (fallback to the standard box model variant) and leaving it out omits Equations (4) and (5). Figure 2 shows a plot of  $\rho^{\text{EOS-80}}(T, S)$ , demonstrating that it is concave in  $S$ . For the experiments using  $\rho^{\text{EOS-80}}$ , we select the initial  $S_i$  such that they lie in the interval  $[5, 15]$  in order to introduce as much nonlinearity as possible into the box model, thereby establishing a stark contrast between experiments with a linear and nonlinear density.

**Linear case.** Following (Tziperman, 2022), we define

$$\Delta S = S_1 - S_2 \quad (6)$$

$$\Delta T = T_1 - T_2 \quad (7)$$

which due to the linearity of differentiation leads to the formulation of the partial differential equations that model the evolution of  $\Delta S$  and  $\Delta T$  under forcings  $F_s$  and  $F_t$  over time, respectively (Tziperman, 2022):

$$\frac{\partial \Delta S}{\partial \tau} = -2 \frac{|q|\Delta S + F_s(\tau)}{V} \quad (8)$$

$$\frac{\partial \Delta T}{\partial \tau} = -2 \frac{|q|\Delta T + F_t(\tau)}{V} \quad (9)$$

where  $V = V_1 = V_2$  is the box volume.

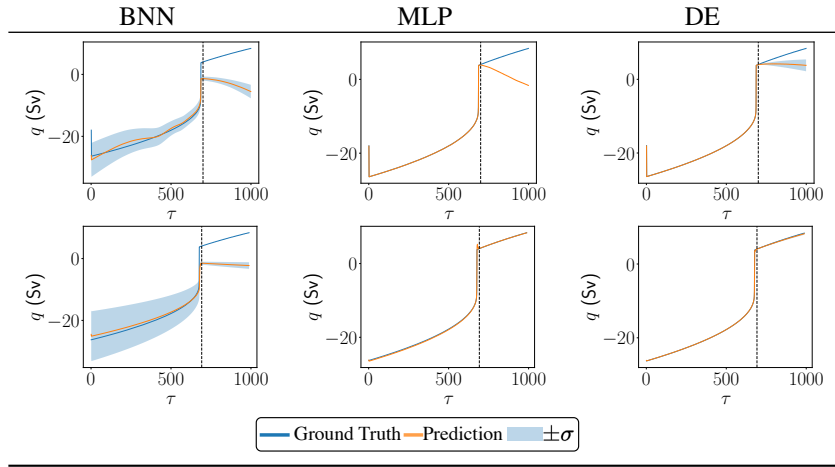


Figure 3. Predictive performance for the considered architectures using physics-informed (PI; first row) and autoregressive (AR; second row) features under  $\mathcal{F}_1$ .

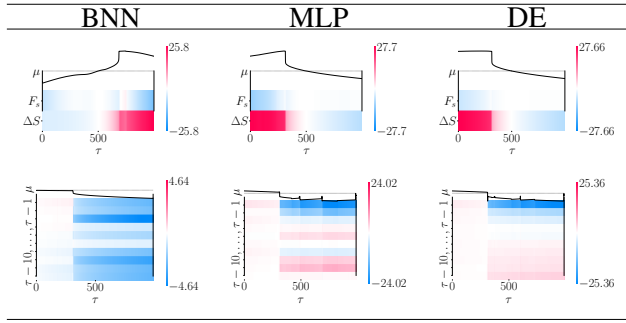


Figure 4. DeepLIFT attribution maps for the considered architectures using physics-informed (PI; top row) and autoregressive (AR; bottom row) features under  $\mathcal{F}_1$ .

Finally,  $q$  is modeled as a proportional density difference between box 1 and 2:

$$q = k(\rho_1 - \rho_2) = \begin{cases} k(\beta\Delta S - \alpha\Delta T), & \rho = \rho^{\text{lin}} \\ k(\rho_1^{\text{EOS-80}} - \rho_2^{\text{EOS-80}}), & \rho = \rho^{\text{EOS-80}} \end{cases} \quad (10)$$

### 2.3. Obtaining Simulated Climate Data with the Stommel Box Model

By solving Equations (8) and (9) or Equations (2) to (5), respectively, we receive sets of values ordered by time:

$$\{\Delta S_\tau\}_{\tau=0}^{\tau_{\max}} \quad \{\Delta T_\tau\}_{\tau=0}^{\tau_{\max}} \quad (11)$$

and

$$\{S_{1,\tau}\}_{\tau=0}^{\tau_{\max}} \quad \{S_{2,\tau}\}_{\tau=0}^{\tau_{\max}} \quad (12)$$

$$\{T_{1,\tau}\}_{\tau=0}^{\tau_{\max}} \quad \{T_{2,\tau}\}_{\tau=0}^{\tau_{\max}} \quad (13)$$

with  $\{F_s(\tau)\}_{\tau=0}^{\tau_{\max}}$  and  $\{F_t(\tau)\}_{\tau=0}^{\tau_{\max}}$  as additional sets of values over time. Note that for the standard box model, we do

not include  $\Delta T$  as an input feature due to the fact that for  $F_t \equiv 0$ ,  $\{\Delta T_\tau\}_{\tau=0}^{\tau_{\max}} \approx \{0\}_{\tau=0}^{\tau_{\max}}$ .

Now let  $f_\theta$  be a neural network with parameters  $\theta$ . We consider two fundamental approaches;

**Approach (I):** Physics-informed (PI), in the sense that the inputs to  $f_\theta$  are physical variables:

$$f_\theta(\Delta S_\tau, \Delta T_\tau, F_s(\tau), F_t(\tau)) = q_\tau \quad (14)$$

and

$$f_\theta(S_{1,\tau}, S_{2,\tau}, T_{1,\tau}, T_{2,\tau}, F_s(\tau), F_t(\tau)) = q_\tau. \quad (15)$$

**Approach (II):** Autoregressive (AR), where we discard the physical variables and predict  $q$  from the last  $\omega$  values of  $q$  in time:

$$f_\theta(q_{\tau-\omega}, \dots, q_{\tau-1}) = q_\tau. \quad (16)$$

### 2.4. Neural Network Architectures

We consider three neural network architectures that we use to predict the AMOC: Multi-Layer Perceptron (MLP), Deep Ensemble (DE) and Bayesian Neural Network (BNN). Only two of the aforementioned architectures are able to quantify uncertainty; the Deep Ensemble by averaging and the BNN by Monte Carlo sampling and successive computation of the mean and standard deviation (Jospin et al., 2022). BNNs have previously been used for ocean applications (Clare & Piggott, 2022; Clare et al., 2022; Yik et al., 2023; Rasouli et al., 2020; Bittig et al., 2018; Juan et al., 2023; Clare & Piggott, 2022), as well as different tasks using them for uncertainty quantification (Thodberg, 1996; Springenberg et al., 2016; Zhang & Garikipati, 2021; Bao et al., 2020). Deep Ensembles consist of training multiple independent deep neural

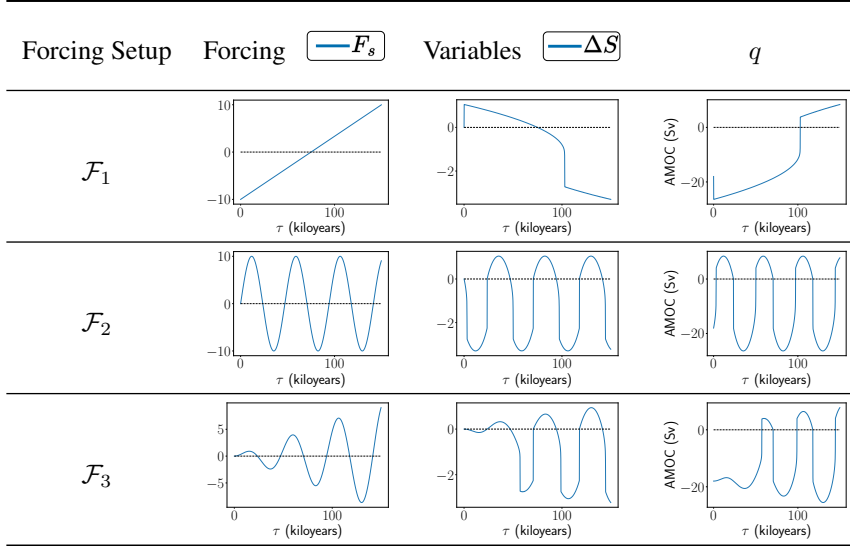


Figure 5. Forcing trajectory, physical variables and AMOC for  $\mathcal{F}_1$ ,  $\mathcal{F}_2$  and  $\mathcal{F}_3$ .

networks whose predictions are averaged during inference. They have been used extensively in climate science applications to generate more accurate predictions (Sonnewald et al., 2021; Cho et al., 2022; Jahanbakht et al., 2021; Qi et al., 2023).

### 2.5. Explainability

Current works (Lobelle et al., 2020; Ditlevsen & Ditlevsen, 2023) on predicting the AMOC focus on predicting the AMOC’s progression over time with an emphasis on a potential tipping point. They do not, however, attempt to explain why their predictive models output the resulting predictions. This is a major restriction with respect to determining *why* the AMOC is projected to evolve in a certain way and impedes climate actionability. We overcome this restriction by generating *feature attributions* per  $\tau$ , visualizing what input feature had a strong contribution for  $q_\tau$ .

We apply DeepLIFT (Shrikumar et al., 2017) and SHAP (Lundberg & Lee, 2017) to each trained  $f_\theta$  in order to determine whether  $f_\theta$  learned the underlying system dynamics or simply imitated the time series  $\{q_\tau\}_{\tau=0}^{\tau_{\max}}$ . For example, in forcing scenarios with the only forcing being  $F_s$ ,  $f_\theta$  should not make a prediction  $\hat{q}_\tau = f_\theta(\dots)$  such that the corresponding attribution  $|\mathcal{A}(\hat{q}_\tau, \Delta S)|$  for  $\Delta S$  is small. This is because salinity differences, induced by the fresh water forcing, drive the AMOC. We chose DeepLIFT in combination with SHAP due to their relative recency among comparable methods (Selvaraju et al., 2016; Ribeiro et al., 2016) and continued impactfulness (Li et al., 2021; Sixt et al., 2020; Zhou et al., 2023; Cakiroglu et al., 2024; Dewi et al., 2023). Besides this, we aim to use different attribution perspectives; sampling feature subsets as well as

propagating internal contribution scores can lead to different attribution maps and tell us something about the internal and external attribution mechanics of a trained predictor, respectively. This can also be seen as examining sensitivity to data vs. the internal network parameters. Prior work (Clare et al., 2022) has examined this, linking different explainability algorithms to aleatoric vs. epistemic uncertainty. Aleatoric uncertainty refers to uncertainty that is inherent in the data whereas epistemic uncertainty denotes uncertainty inherent in the model that is being used (Clare et al., 2022). For the autoregressive cases (using SHAP) due to an input length of 10, we do not use all feature subsets but rather sample them. We repeat this sampling process 20 times and take the mean for each  $\tau$  in each attribution map.

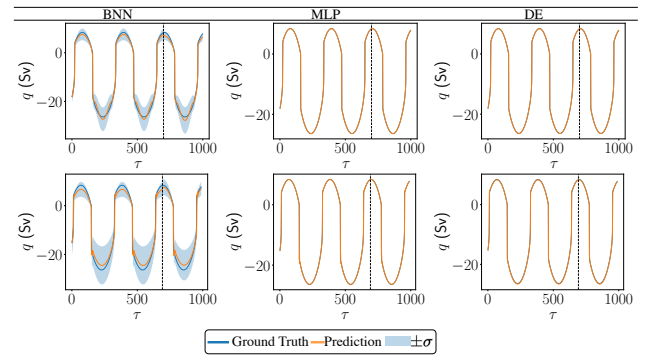


Figure 6. Predictive performance for the considered architectures using physics-informed (PI; first row) and autoregressive (AR; second row) features under  $\mathcal{F}_2$ .

## 2.6. Detecting Network Understanding vs. Imitation

One question we address is whether  $f_\theta$  learned or imitated the physics of  $q$ . Although there exists no formal method of identifying  $f_\theta$ 's understanding of physics, we can infer some physical understanding and imitation by identifying cases in which a plausible physical understanding was learned vs. when spurious correlations were learned. Mainly, if  $\Delta S$  or  $S_i$  receive high absolute attribution scores, we can infer learned physics as well as an attribution pattern assigning  $S_1$  a score with polarity  $a \in \{-1, 1\}$  and  $S_2$  a score with polarity  $-a$ . This would concur with natural AMOC dynamics; differences in salinity cause differences in density which then drive  $q$ .

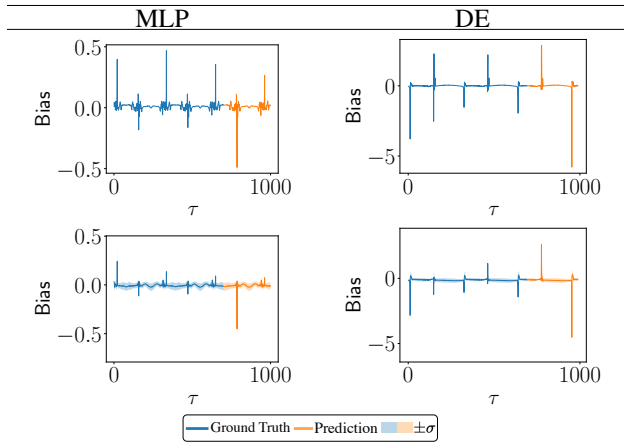


Figure 7. Bias ( $\hat{q}_\tau - q_\tau$ ) for the MLP and DE architectures under  $\mathcal{F}_2$ .

## 3. Experiments

### 3.1. Experimental Design

We aim to understand two perspectives: how does the AMOC evolve according to the physical ruleset proposed in Section 2.2 vs. autoregressively where we only use measured data that is sampled from an externally observable physical process? On the macro level, we have the difference between a linear box model ( $\rho^{\text{lin}}$ ) and a nonlinear one ( $\rho^{\text{EOS-80}}$ ) which yields a more accurate but difficult-to-predict AMOC representation.

In Table 1, we list the combinations of forcings we use in our experiments. For the standard box model we set  $\rho = \rho^{\text{lin}}$  and include a linear and two sinusoidal forcings with one nonstationary forcing. For the extended box model, we consider the same forcings in conjunction with  $F_t$  and  $\rho = \rho^{\text{EOS-80}}$ . All forcings with their corresponding  $\Delta\{S, T\}$  and  $\{S_i, T_i\}$  including the resulting AMOC are plotted in Figures 5 and 9, respectively. We train all models for 120 epochs using the Adam optimizer (Kingma & Ba, 2014).

### 3.2. Results

Here, we only include the DeepLIFT attribution plots while the SHAP plots are located in Appendix B due to space constraints and their similarity to the DeepLIFT attributions. The resulting ground-truth-prediction plots after 120 epochs of training are plotted in Figures 3, 6, 10, 13, 15 and 18 with DeepLIFT attribution heatmaps being plotted in Figures 4, 8, 12, 14, 17 and 20. A vertical dashed line indicates the train/test split (70% / 30%). We supply plots of the bias  $\hat{q}_\tau - q_\tau$  for  $\{\mathcal{F}_2, \mathcal{F}_3, \mathcal{F}_5, \mathcal{F}_6\}$  in Figures 7, 11, 16 and 19. We conduct additional tuning experiments on the BNN in Appendix E.

In Figures 3 and 4, we plot the predictions and ground truth with uncertainty bands under  $\mathcal{F}_1$ . Immediately, we notice that the BNN architecture results in highly uncertain predictions with both physics-informed (PI) and autoregressive (AR) features. This is not the case for the MLP and DE, the latter of which recovers the best approximation for the validation data. In the physics-informed case, we notice slight uncertainty where the MLP is producing divergent predictions. Autoregressively, we notice a small spike in the predicted AMOC (compare bottom row of Figure 3) that is dampened using a DE. This is likely indicative of a failed tipping point capture since these spikes occur just around the recovery of the only tipping point present in the data. The attribution maps under physics-informed features are fairly similar up to a sign flip in the attributions, which comes from different random initializations of the models. Where there are physically plausible attributions in the physics-informed case, the autoregressive differ significantly between the BNN and the dense architectures; while the dense architectures primarily use the feature subset  $\{\tau - 3, \dots, \tau - 1\}$ , the BNN appears to pick up spurious correlations even in a simple linear forcing scenario, indicating that it likely did not develop a plausible physical understanding.

Concerning predictive performance under  $\mathcal{F}_2$  (see Figure 6), we have the BNN failing to accurately articulate all of the tipping points under stationarity (physics-informed and autoregressively). Instead, it smoothly approximates breakdown and recovery phases with a large amount of uncertainty. The MLP and DE perform remarkably well using both PI and AR data and have seemingly equal performance. However, from Figure 7 it becomes clear that the DE performs better due to a smaller and smoother bias which also reflects in the attributions (Figure 8); smoother transitions in  $\Delta S$  as well as  $\{\tau - 3, \dots, \tau - 1\}$ .

Under  $\mathcal{F}_3$ , we notice an interesting failure to capture an out-of-sample tipping point breakdown and its recovery (compare top row of Figure 10) with PI data. Interestingly, this is consistent among all three architectures and thus raises the question of whether a system under nonstationary

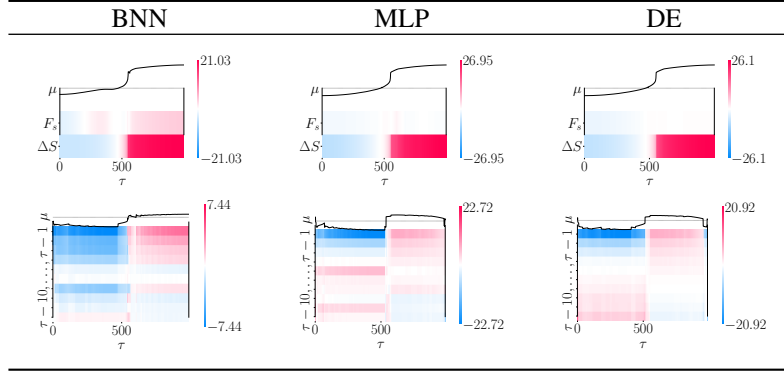


Figure 8. DeepLIFT attribution maps for the considered architectures using physics-informed (PI; top row) and autoregressive (AR; bottom row) features under  $\mathcal{F}_2$ .

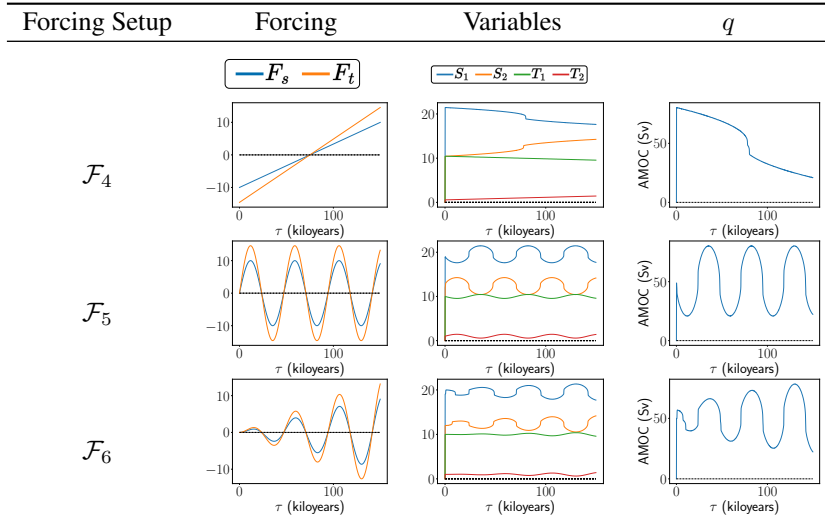


Figure 9. Forcing trajectory, physical variables and AMOC for  $\mathcal{F}_4$ ,  $\mathcal{F}_5$  and  $\mathcal{F}_6$ .

forcing is too complex for neural networks to represent. However, the DE allows for a slight amount of uncertainty in this particular tipping point. In the AR case, the BNN generates profusely uncertain outputs during the recovery of a tipping point and displays a consistent positive shift in the AMOC. Performance between the MLP and Deep Ensemble appears equal up to a bias (see Figure 11) which is smoothed with PI data but tends to be larger than the MLP’s with AR data. Curiously, the BNN leaves out ranges of AR features (compare Figure 12, bottom row) in its prediction which could indicate that it simply learned to approximate a rough estimate of  $q$  while leaving out certain features. This hypothesis arises due to the dense architectures having most of their attribution scores distributed among the feature range  $\{\tau - 2, \tau - 1\}$ , while attaining good generalization abilities.

In the more complicated  $\mathcal{F}_4$ , which requires significantly more input variables, the BNN architecture tends to produce a version of the AMOC that either diverges (see Figure 13,

top row) or is shifted (see Figure 13, bottom row). This is linked to a large amount of spuriously picked up features (see Figure 14, first row) with PI and AR data. In particular, the MLP and DE approximate  $q$  well under  $\mathcal{F}_4$  with a significantly smaller number of attributed features (see Figure 14), which is a likely indication that these architectures learned the physics of the AMOC.

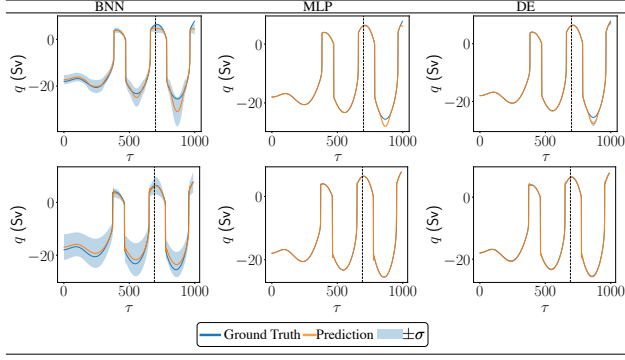


Figure 10. Predictive performance for the considered architectures using physics-informed (PI; first row) and autoregressive (AR; second row) features under  $\mathcal{F}_3$ .

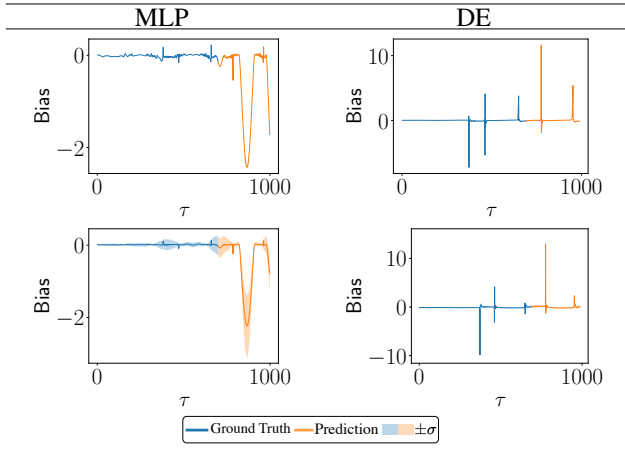


Figure 11. Bias ( $\hat{q}_\tau - q_\tau$ ) for the MLP and DE architectures under  $\mathcal{F}_3$ .

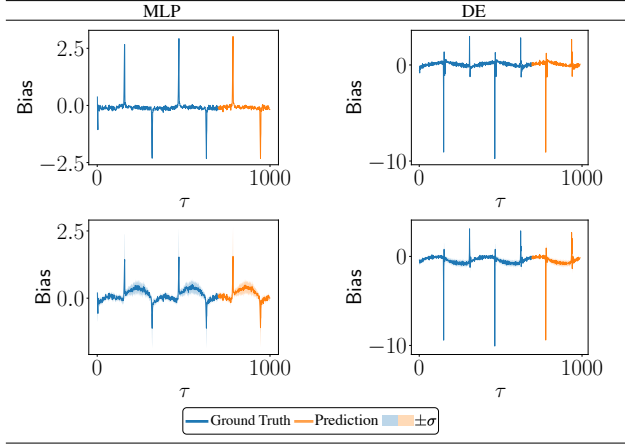


Figure 16. Bias ( $\hat{q}_\tau - q_\tau$ ) for the MLP and DE architectures under  $\mathcal{F}_5$ .

Under  $\mathcal{F}_5$ , the BNN architecture significantly simplifies the AMOC and tends to approximate it by a nearly constant

function during recovery periods. This is paired with high uncertainties during the tipping points for AR data (compare Figure 15). It is likely that this stems from the BNN picking up additional spurious correlations (see Figure 17, left column) which the dense architectures do not pick up. Interestingly, it appears that salinity is the main driver of the AMOC in highly nonlinear and extreme climate scenarios (compare Figure 17, row 2 and 3). In contrast to the BNN architecture, the MLP and DE architectures are good at handling both PI and AR data, with the ensemble’s bias tending towards zero (see Figure 16). With respect to  $\mathcal{F}_6$ , a slightly misaligned tipping point in the validation set is observed (see Figure 18, top row), although it is dampened by the Ensemble architecture. With AR data, the BNN appears to have learned a vertically negatively shifted version of the AMOC (see Figure 18, bottom row) that is not learned by the other architectures. Curiously, the misaligned tipping point is not revealed by the attribution maps (Figure 20). It is, however, shown that the BNN obtained correlations from a number of features which does not seem to be necessary to learn an accurate physical understanding of the AMOC. A further observation is that the bias for both MLP and ensemble is the same in this forcing scenario.

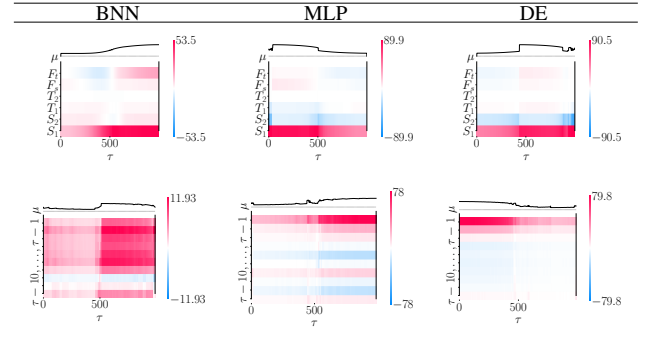


Figure 17. DeepLIFT attribution maps for the considered architectures using physics-informed (PI; top row) and autoregressive (AR; bottom row) features under  $\mathcal{F}_5$ .

We see that adjusting the prior standard deviation (Appendix E) of the BNN leads to a diverse set of outcomes with respect to predictive performance and explainability. For example, in  $\mathcal{F}_1$  (see Figure 27) with PI data, none of the values of  $\sigma$  can produce very accurate predictions. Pathological cases in which the prediction is near-constant show almost vanishing attributions (Figure 28 (e, f, o, p, q, r)). Interestingly, the amount of failure cases with near-constant predictions when varying  $\sigma$  is equal across equal density approximations; in  $\mathcal{F}_1$ ,  $\mathcal{F}_2$  and  $\mathcal{F}_3$ , there are exactly three such cases (compare Figures 27, 29 and 31) while in  $\mathcal{F}_4$ ,  $\mathcal{F}_5$  and  $\mathcal{F}_6$  there are exactly two (compare Figures 33, 35 and 37). These occur for very low values of  $\sigma$  in which the BNN is unable to sample appropriately.

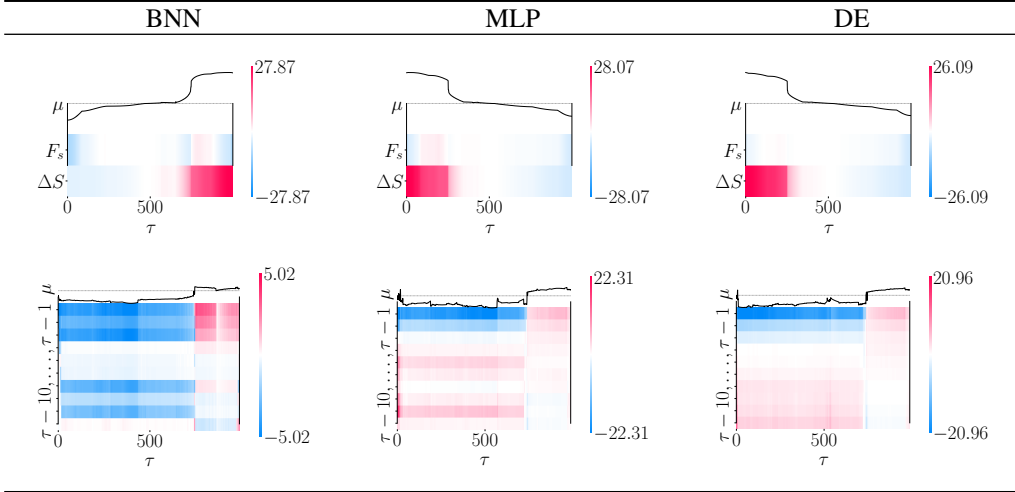


Figure 12. DeepLIFT attribution maps for the considered architectures using physics-informed (PI; top row) and autoregressive (AR; bottom row) features under  $\mathcal{F}_3$ .

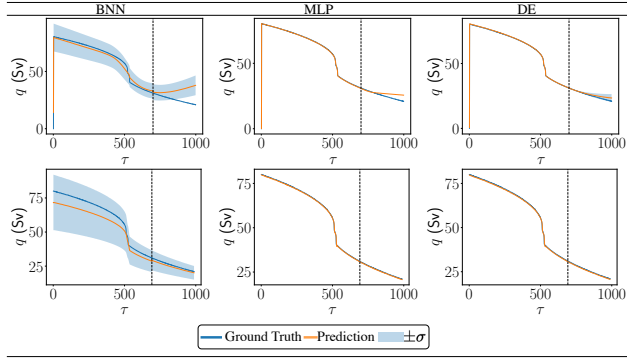


Figure 13. Predictive performance for the considered architectures using physics-informed (PI; first row) and autoregressive (AR; second row) features under  $\mathcal{F}_4$ .

### 4. Conclusion & Future Work

In this paper, we have addressed the question of whether neural networks are able to learn the underlying physical system of the AMOC or entirely derive predictive skill from “unphysical” or spurious correlations. In both the physics-informed and autoregressive approach, the BNN architecture is unable to approximate the AMOC sufficiently well (compare Figures 3, 6, 10, 13, 15 and 18). It is unlikely that these results make an absolute statement about the capabilities of BNNs but rather tell us that they are more sensitive to careful hyperparameter tuning than other architectures. As shown in Appendix E, the BNN is able to capture the AMOC but only after tuning another parameter. Especially its imposed latent space regularization could be a crucial factor with respect to its predictive performance. Using the BNN architecture autoregressively leads to it picking up spurious correlations which is unwanted and indicates failure to

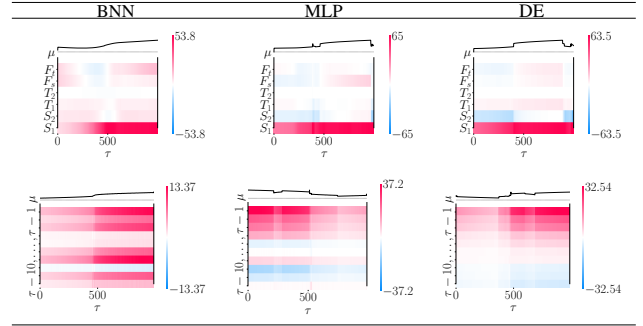


Figure 14. DeepLIFT attribution maps for the considered architectures using physics-informed (PI; top row) and autoregressive (AR; bottom row) features under  $\mathcal{F}_4$ .

learn the AMOC physics. Such spurious correlations are not seen in the dense architectures, leading us to the conclusion that these learned a sensible representation of the AMOC’s physics. Apart from this, the BNN appears to produce a consistently negative shift in the  $y$ -axis for autoregressive data which is again not observed in the MLP and DE. In general, both dense architectures (MLP & DE) generalize better, possibly due to the better attractor space optimization which is seen especially in the DE. Both architectures’ ability to perform well out-of-sample is, other than in the BNNs, another plausible indicator that they retained AMOC physics during training. Importantly, due to the spiking behavior near imminent breakdown and recovery phases in AR data, we raise concern about the catastrophic predictions made using the methodologies of Ditlevsen & Ditlevsen (2023) and emphasize that our approach makes fewer assumptions that would bias an effective AMOC forecast. In the future, we see the need for experiments on more forcing scenarios, especially those that represent current greenhouse gas emis-

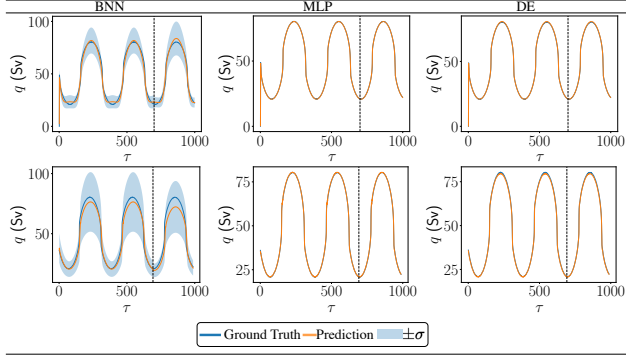


Figure 15. Predictive performance for the considered architectures using physics-informed (PI; first row) and autoregressive (AR; second row) features under  $\mathcal{F}_5$ .

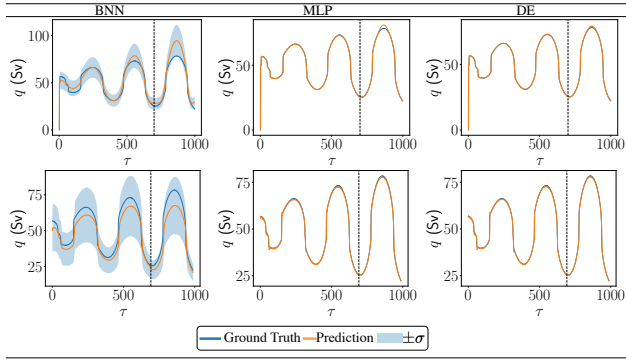


Figure 18. Predictive performance for the considered architectures using physics-informed (PI; first row) and autoregressive (AR; second row) features under  $\mathcal{F}_6$ .

sions and fresh water forcing in the North Atlantic Ocean. Besides this, different neural network architectures like the FNO or Graph Neural Networks (GNNs; (Scarselli et al., 2008)) could be applied to predict  $q$ , however, without the ready ability to apply XAI.

### Acknowledgements

We thank Mariana Clare and Redouane Lguensat for their helpful comments.

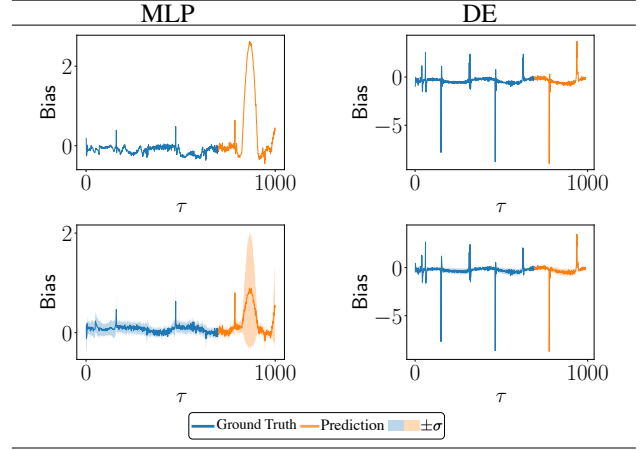


Figure 19. Bias ( $\hat{q}_\tau - q_\tau$ ) for the MLP and DE architectures under  $\mathcal{F}_6$ .

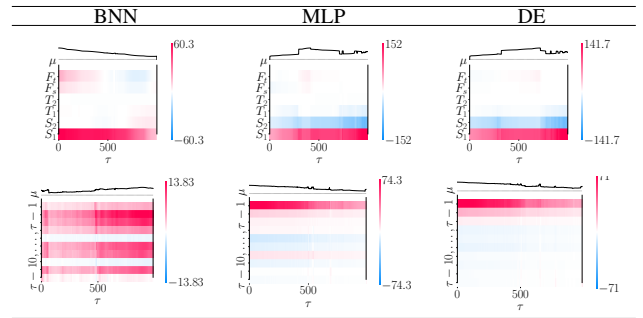


Figure 20. DeepLIFT attribution maps for the considered architectures using physics-informed (PI; top row) and autoregressive (AR; bottom row) features under  $\mathcal{F}_6$ .

## References

- Bao, Y., Velni, J. M., and Shahbakhti, M. Epistemic uncertainty quantification in state-space l<sub>p</sub>v model identification using bayesian neural networks. *IEEE Control Systems Letters*, 5(2):719–724, 2020.
- Bire, S., Lütjens, B., Azizzadenesheli, K., Anandkumar, A., and Hill, C. N. Ocean emulation with fourier neural operators: Double gyre. *Authorea Preprints*, 2023.
- Bittig, H. C., Steinhoff, T., Claustre, H., Fiedler, B., Williams, N. L., Sauzède, R., Körtzinger, A., and Gattuso, J.-P. An alternative to static climatologies: Robust estimation of open ocean co<sub>2</sub> variables and nutrient concentrations from t, s, and o<sub>2</sub> data using bayesian neural networks. *Frontiers in Marine Science*, 5:328, 2018.
- Cakiroglu, C., Demir, S., Ozdemir, M. H., Aylak, B. L., Sariisik, G., and Abualigah, L. Data-driven interpretable ensemble learning methods for the prediction of wind turbine power incorporating shap analysis. *Expert Systems with Applications*, 237:121464, 2024.
- Cheng, W., Chiang, J. C., and Zhang, D. Atlantic meridional overturning circulation (amoc) in cmip5 models: Rcp and historical simulations. *Journal of Climate*, 26(18):7187–7197, 2013.
- Cho, D., Yoo, C., Son, B., Im, J., Yoon, D., and Cha, D.-H. A novel ensemble learning for post-processing of nwp model’s next-day maximum air temperature forecast in summer using deep learning and statistical approaches. *Weather and Climate Extremes*, 35:100410, 2022.
- Clare, M. C. and Piggott, M. D. Bayesian neural networks for the probabilistic forecasting of wind direction and speed using ocean data. *Trends in Renewable Energies Offshore*, pp. 533–540, 2022.
- Clare, M. C., Sonnewald, M., Lguensat, R., Deshayes, J., and Balaji, V. Explainable artificial intelligence for bayesian neural networks: toward trustworthy predictions of ocean dynamics. *Journal of Advances in Modeling Earth Systems*, 14(11):e2022MS003162, 2022.
- Dewi, C., CHEN, R.-C., Yu, H., and JIANG, X. Xai for image captioning using shap. *Journal of Information Science & Engineering*, 39(4), 2023.
- Ditlevsen, P. and Ditlevsen, S. Warning of a forthcoming collapse of the atlantic meridional overturning circulation. *Nature Communications*, 14(1):1–12, 2023.
- Fofonoff, N. Physical properties of seawater: A new salinity scale and equation of state for seawater. *Journal of Geophysical Research: Oceans*, 90(C2):3332–3342, 1985.
- Hazeleger, W., Wouters, B., van Oldenborgh, G. J., Corti, S., Palmer, T., Smith, D., Dunstone, N., Kröger, J., Pohlmann, H., and von Storch, J.-S. Predicting multiyear north atlantic ocean variability. *Journal of Geophysical Research: Oceans*, 118(3):1087–1098, 2013.
- Irrgang, C., Boers, N., Sonnewald, M., Barnes, E. A., Kadow, C., Staneva, J., and Saynisch-Wagner, J. Towards neural earth system modelling by integrating artificial intelligence in earth system science. *Nature Machine Intelligence*, 3(8):667–674, 2021.
- Jackson, L. C., Hewitt, H. T., Bruciaferri, D., Calvert, D., Graham, T., Guiavarc’h, C., Menary, M. B., New, A. L., Roberts, M., and Storkey, D. Challenges simulating the amoc in climate models. *Philosophical Transactions of the Royal Society A*, 381(2262):20220187, 2023.
- Jahanbakht, M., Xiang, W., and Azghadi, M. R. Sea surface temperature forecasting with ensemble of stacked deep neural networks. *IEEE Geoscience and Remote Sensing Letters*, 19:1–5, 2021.
- Jones, N. How machine learning could help to improve climate forecasts. *Nature*, 548(7668), 2017.
- Jospin, L. V., Laga, H., Boussaid, F., Buntine, W., and Bennamoun, M. Hands-on bayesian neural networks—a tutorial for deep learning users. *IEEE Computational Intelligence Magazine*, 17(2):29–48, 2022.
- Juan, N. P., Matutano, C., and Valdecantos, V. N. Uncertainties in the application of artificial neural networks in ocean engineering. *Ocean Engineering*, 284:115193, 2023.
- Kingma, D. P. and Ba, J. Adam: A method for stochastic optimization. *arXiv preprint arXiv:1412.6980*, 2014.
- Lenton, T. M., Held, H., Kriegler, E., Hall, J. W., Lucht, W., Rahmstorf, S., and Schellnhuber, H. J. Tipping elements in the earth’s climate system. *Proceedings of the National Academy of Sciences*, 105(6):1786–1793, 2008.
- Li, J., Zhang, C., Zhou, J. T., Fu, H., Xia, S., and Hu, Q. Deep-lift: Deep label-specific feature learning for image annotation. *IEEE Transactions on Cybernetics*, 52(8):7732–7741, 2021.
- Li, Z., Kovachki, N., Azizzadenesheli, K., Liu, B., Bhattacharya, K., Stuart, A., and Anandkumar, A. Fourier neural operator for parametric partial differential equations. *arXiv preprint arXiv:2010.08895*, 2020.
- Liu, W., Xie, S.-P., Liu, Z., and Zhu, J. Overlooked possibility of a collapsed atlantic meridional overturning circulation in warming climate. *Science Advances*, 3(1):e1601666, 2017.

- Lobelle, D., Beaulieu, C., Livina, V., Sevellec, F., and Frajka-Williams, E. Detectability of an amoc decline in current and projected climate changes. *Geophysical Research Letters*, 47(20):e2020GL089974, 2020.
- Lundberg, S. M. and Lee, S.-I. A unified approach to interpreting model predictions. *Advances in Neural Information Processing Systems*, 30, 2017.
- Mahajan, S., Zhang, R., Delworth, T. L., Zhang, S., Rosati, A. J., and Chang, Y.-S. Predicting atlantic meridional overturning circulation (amoc) variations using subsurface and surface fingerprints. *Deep Sea Research Part II: Topical Studies in Oceanography*, 58(17-18):1895–1903, 2011.
- Matei, D., Baehr, J., Jungclaus, J. H., Haak, H., Müller, W. A., and Marotzke, J. Multiyear prediction of monthly mean atlantic meridional overturning circulation at 26.5 n. *Science*, 335(6064):76–79, 2012.
- McCarthy, G. D., Smeed, D. A., Johns, W. E., Frajka-Williams, E., Moat, B. I., Rayner, D., Baringer, M. O., Meinen, C. S., Collins, J., and Bryden, H. L. Measuring the atlantic meridional overturning circulation at 26 n. *Progress in Oceanography*, 130:91–111, 2015.
- Menary, M. B., Roberts, C. D., Palmer, M. D., Halloran, P. R., Jackson, L., Wood, R. A., Müller, W. A., Matei, D., and Lee, S.-K. Mechanisms of aerosol-forced amoc variability in a state of the art climate model. *Journal of Geophysical Research: Oceans*, 118(4):2087–2096, 2013.
- Pathak, J., Subramanian, S., Harrington, P., Raja, S., Chattopadhyay, A., Mardani, M., Kurth, T., Hall, D., Li, Z., Azizzadenesheli, K., et al. FourCastNet: A global data-driven high-resolution weather model using adaptive fourier neural operators. *arXiv preprint arXiv:2202.11214*, 2022.
- Qi, J., Zhang, L., Yin, B., Li, D., Xie, B., and Sun, G. Advancing ocean subsurface thermal structure estimation in the pacific ocean: A multi-model ensemble machine learning approach. *Dynamics of Atmospheres and Oceans*, 104:101403, 2023.
- Rasouli, K., Nasri, B. R., Soleymani, A., Mahmood, T. H., Hori, M., and Haghighi, A. T. Forecast of streamflows to the arctic ocean by a bayesian neural network model with snowcover and climate inputs. *Hydrology Research*, 51(3):541–561, 2020.
- Ribeiro, M. T., Singh, S., and Guestrin, C. "why should i trust you?" explaining the predictions of any classifier. In *Proceedings of the 22nd ACM SIGKDD international conference on knowledge discovery and data mining*, pp. 1135–1144, 2016.
- Salman, A. G., Kanigoro, B., and Heryadi, Y. Weather forecasting using deep learning techniques. In *2015 international conference on advanced computer science and information systems (ICACSIS)*, pp. 281–285. IEEE, 2015.
- Scarselli, F., Gori, M., Tsoi, A. C., Hagenbuchner, M., and Monfardini, G. The graph neural network model. *IEEE Transactions on Neural Networks*, 20(1):61–80, 2008.
- Selvaraju, R. R., Cogswell, M., Das, A., Vedantam, R., Parikh, D., and Batra, D. Grad-cam: Visual explanations from deep networks via gradient-based localization. *arXiv preprint arXiv:1610.02391*, 2016.
- Shrikumar, A., Greenside, P., and Kundaje, A. Learning important features through propagating activation differences. In *International Conference on Machine Learning*, pp. 3145–3153. PMLR, 2017.
- Singh, N., Chaturvedi, S., and Akhter, S. Weather forecasting using machine learning algorithm. In *2019 International Conference on Signal Processing and Communication (ICSC)*, pp. 171–174. IEEE, 2019.
- Sixt, L., Granz, M., and Landgraf, T. When explanations lie: Why many modified bp attributions fail. In *International Conference on Machine Learning*, pp. 9046–9057. PMLR, 2020.
- Sonnewald, M. and Lguensat, R. Revealing the impact of global heating on north atlantic circulation using transparent machine learning. *Journal of Advances in Modeling Earth Systems*, 13(8):e2021MS002496, 2021.
- Sonnewald, M., Lguensat, R., Jones, D. C., Dueben, P. D., Brajard, J., and Balaji, V. Bridging observations, theory and numerical simulation of the ocean using machine learning. *Environmental Research Letters*, 16(7):073008, 2021.
- Springenberg, J. T., Klein, A., Falkner, S., and Hutter, F. Bayesian optimization with robust bayesian neural networks. *Advances in neural information processing systems*, 29, 2016.
- Stommel, H. Thermohaline convection with two stable regimes of flow. *Tellus*, 13(2):224–230, 1961.
- Swingedouw, D., Mignot, J., Labetoulle, S., Guilyardi, E., and Madec, G. Initialisation and predictability of the amoc over the last 50 years in a climate model. *Climate Dynamics*, 40(9-10):2381–2399, 2013.
- Thodberg, H. H. A review of bayesian neural networks with an application to near infrared spectroscopy. *IEEE transactions on Neural Networks*, 7(1):56–72, 1996.

- Thomas, M. D. and Fedorov, A. V. Mechanisms and impacts of a partial amoc recovery under enhanced freshwater forcing. *Geophysical Research Letters*, 46(6):3308–3316, 2019.
- Tziperman, E. *Global Warming Science: A Quantitative Introduction to Climate Change and its Consequences*. Princeton University Press, 2022.
- Van Nes, E. H., Arani, B. M., Staal, A., van der Bolt, B., Flores, B. M., Bathiany, S., and Scheffer, M. What do you mean, 'tipping point'? *Trends in Ecology & Evolution*, 31(12):902–904, 2016.
- Wen, N., Frankignoul, C., and Gastineau, G. Active amoc-nao coupling in the ipsl-cm5a-mr climate model. *Climate Dynamics*, 47:2105–2119, 2016.
- Yik, W., Sonnewald, M., Clare, M. C., and Lguensat, R. Southern ocean dynamics under climate change: New knowledge through physics-guided machine learning. *arXiv preprint arXiv:2310.13916*, 2023.
- Zhang, X. and Garikipati, K. Bayesian neural networks for weak solution of pdes with uncertainty quantification. *arXiv preprint arXiv:2101.04879*, 2021.
- Zhou, X., Liu, C., Zhai, L., Jia, Z., Guan, C., and Liu, Y. Interpretable and robust ai in eeg systems: A survey. *arXiv preprint arXiv:2304.10755*, 2023.

### A. Box Model Parameters

We show the parameter configuration for the Stommel box model in this paper.

Parameter	Value
$S_0$	35.0 ppt
$T_0$	24.0 °C
$S_1$	12.0 ppt
$S_2$	20.0 ppt
$T_1$	1.0 °C
$T_2$	10.0 °C
$A$ (area)	$(5 \times 10^7)$ m <sup>2</sup>
$k$	$1 \times 10^{10}$
Depth	4000 m
$\alpha$	0.2
$\beta$	0.8
Years of prediction	150,000

Table 2. Parameters for the box model used in our analysis.

### B. SHAP Attributions

We present additional attribution plots given by the SHAP algorithm. These concur narrowly with the DeepLIFT attribution plots.

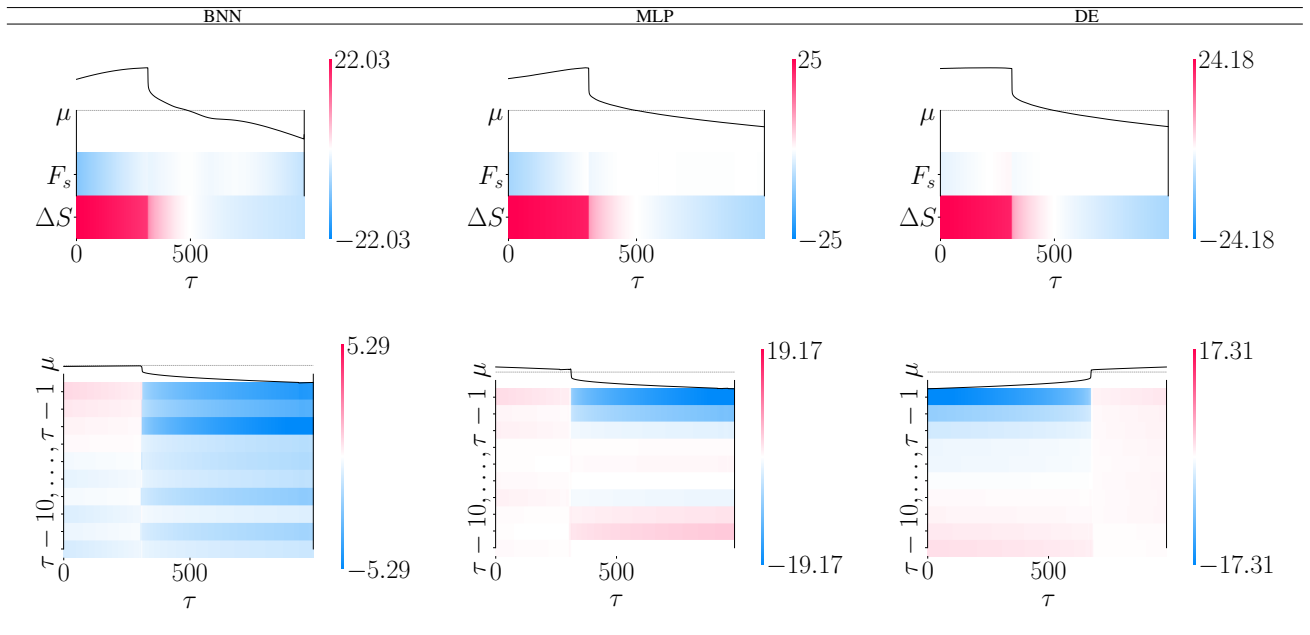


Figure 21. SHAP attribution maps for the considered architectures using physics-informed (PI; top row) and autoregressive (AR; bottom row) features under  $\mathcal{F}_1$ .

The Importance of Architecture Choice in Deep Learning for Climate Applications

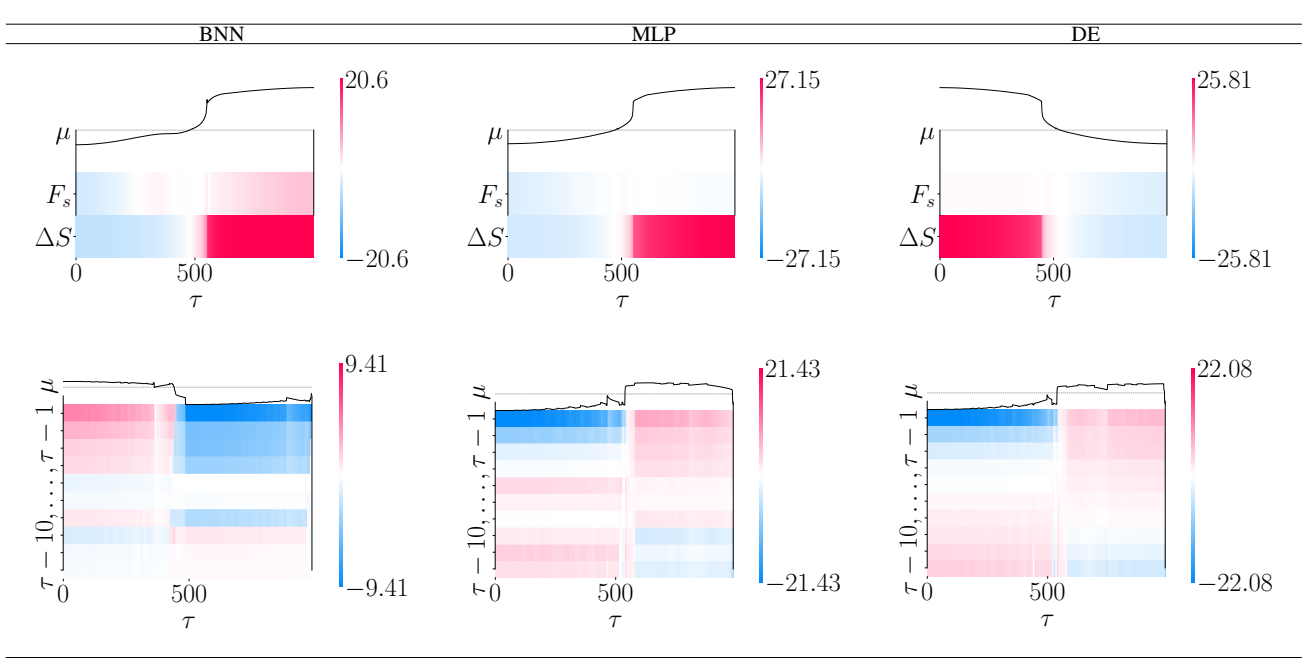


Figure 22. SHAP attribution maps for the considered architectures using physics-informed (PI; top row) and autoregressive (AR; bottom row) features under  $\mathcal{F}_2$ .

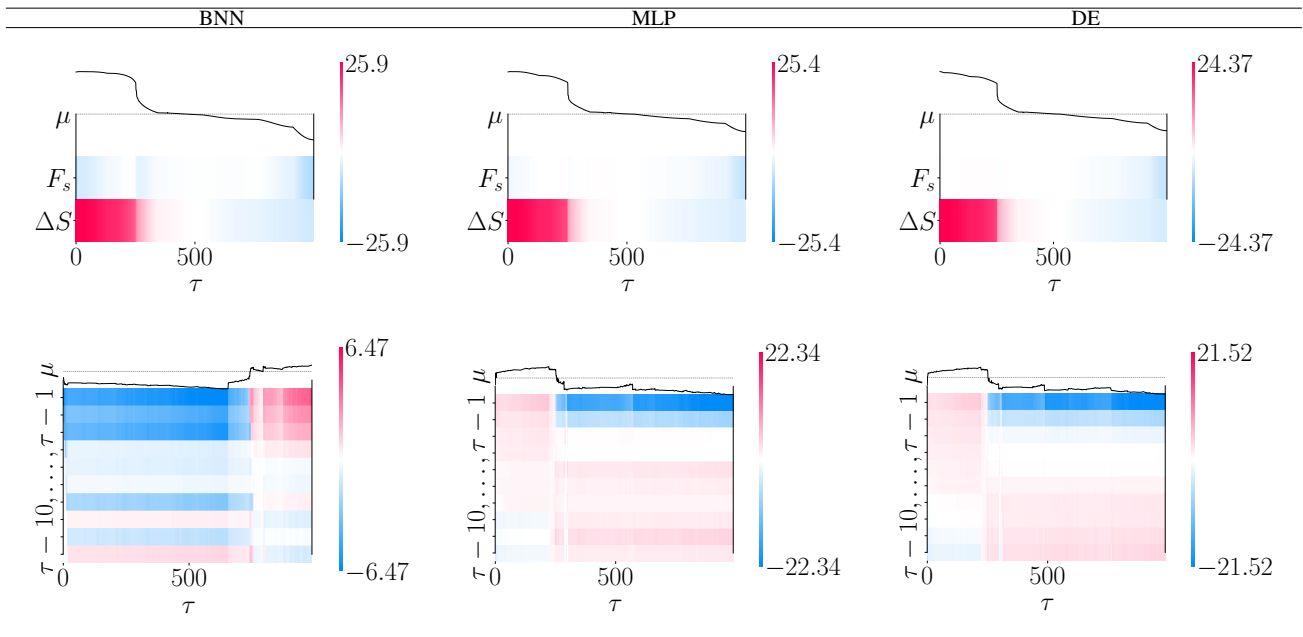


Figure 23. SHAP attribution maps for the considered architectures using physics-informed (PI; top row) and autoregressive (AR; bottom row) features under  $\mathcal{F}_3$ .

## The Importance of Architecture Choice in Deep Learning for Climate Applications

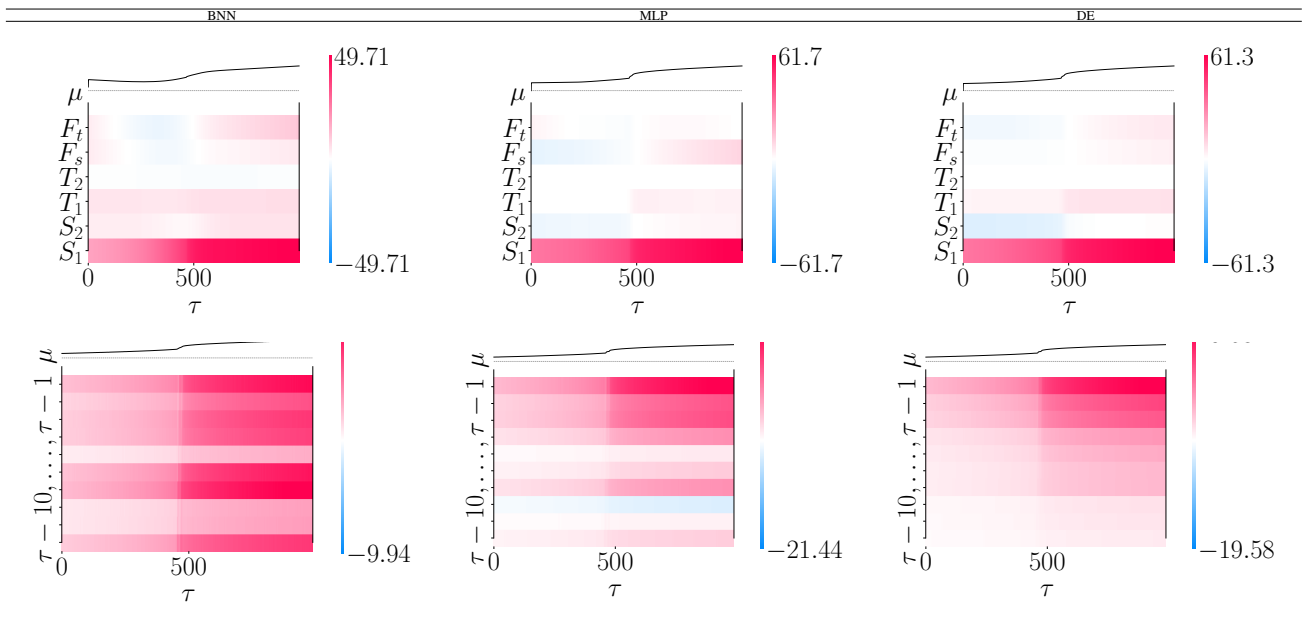


Figure 24. SHAP attribution maps for the considered architectures using physics-informed (PI; top row) and autoregressive (AR; bottom row) features under  $\mathcal{F}_4$ .

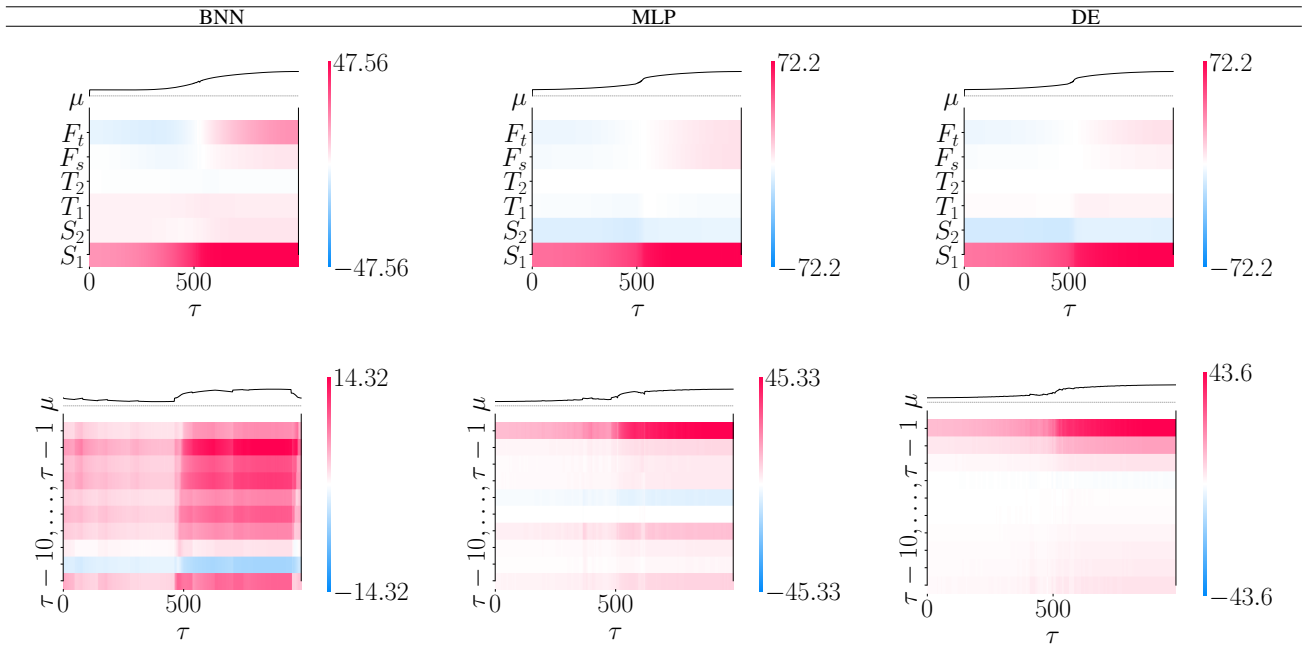


Figure 25. SHAP attribution maps for the considered architectures using physics-informed (PI; top row) and autoregressive (AR; bottom row) features under  $\mathcal{F}_5$ .

# The Importance of Architecture Choice in Deep Learning for Climate Applications

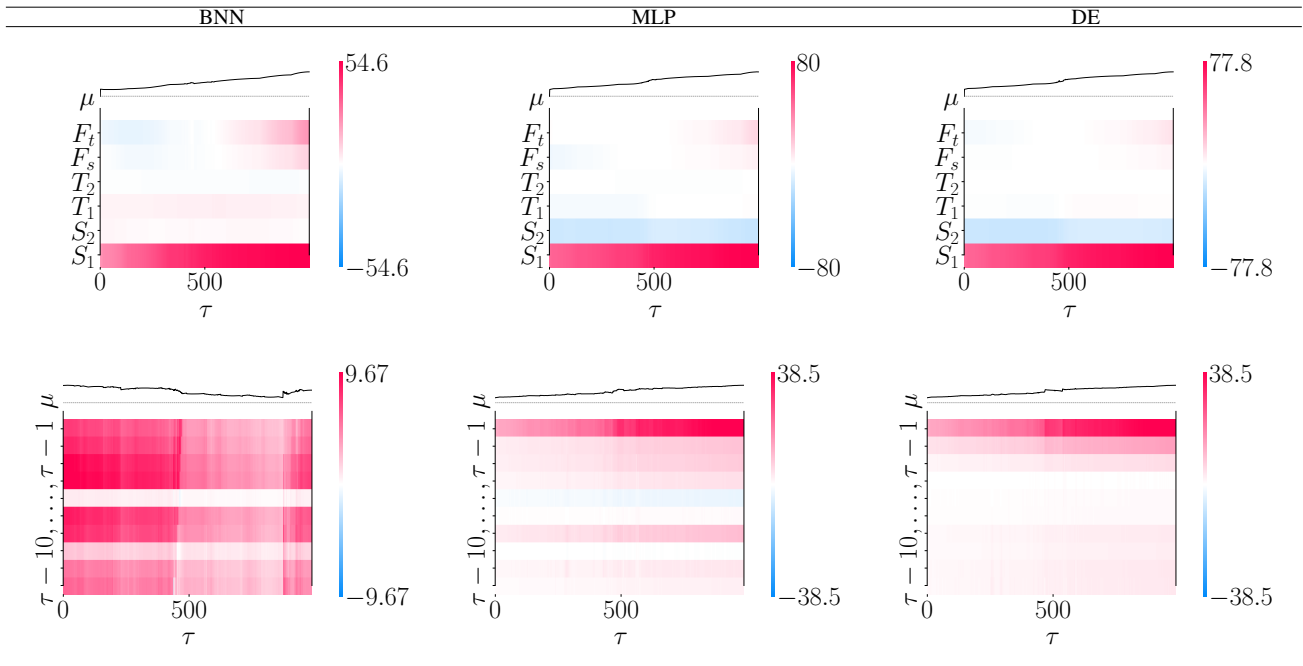


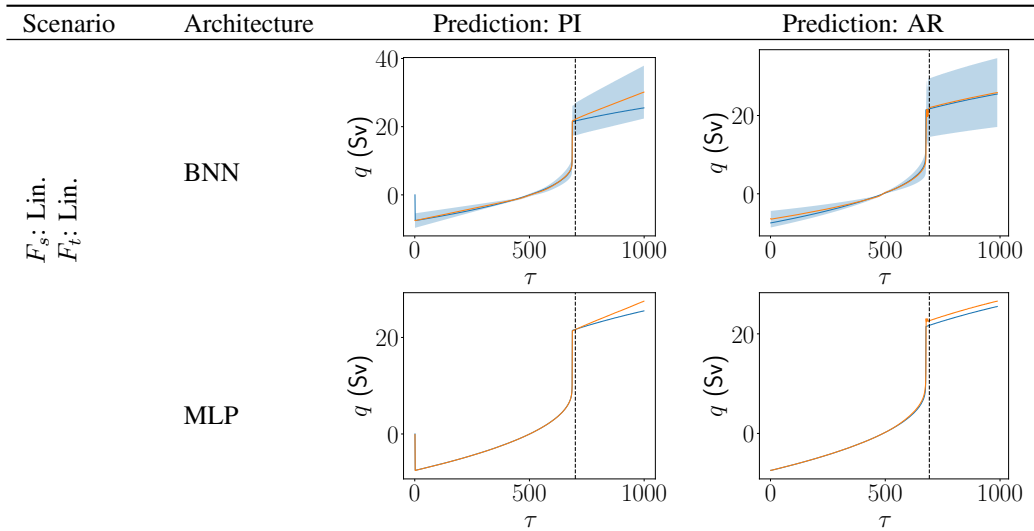
Figure 26. SHAP attribution maps for the considered architectures using physics-informed (PI; top row) and autoregressive (AR; bottom row) features under  $\mathcal{F}_6$ .

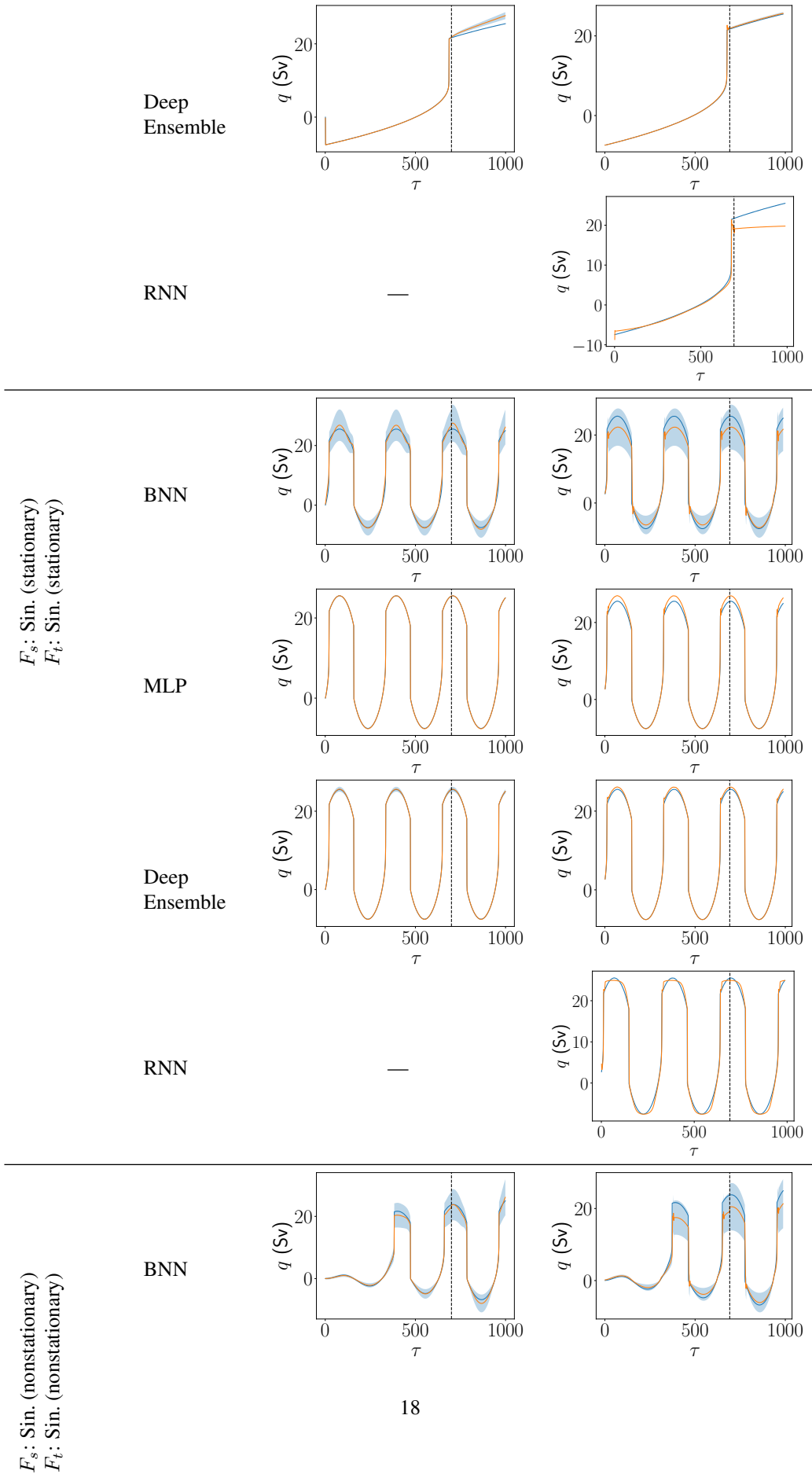
## C. $\rho^{\text{lin}}$

In this Appendix, we include supplementary forcing scenarios using  $\rho^{\text{lin}}$  that complement  $\{\mathcal{F}_1, \dots, \mathcal{F}_6\}$  from the main experiments. We include a Recurrent Neural Network (RNN) as an additional architecture.

### C.1. Extended Box Model

#### C.1.1. PERFORMANCE





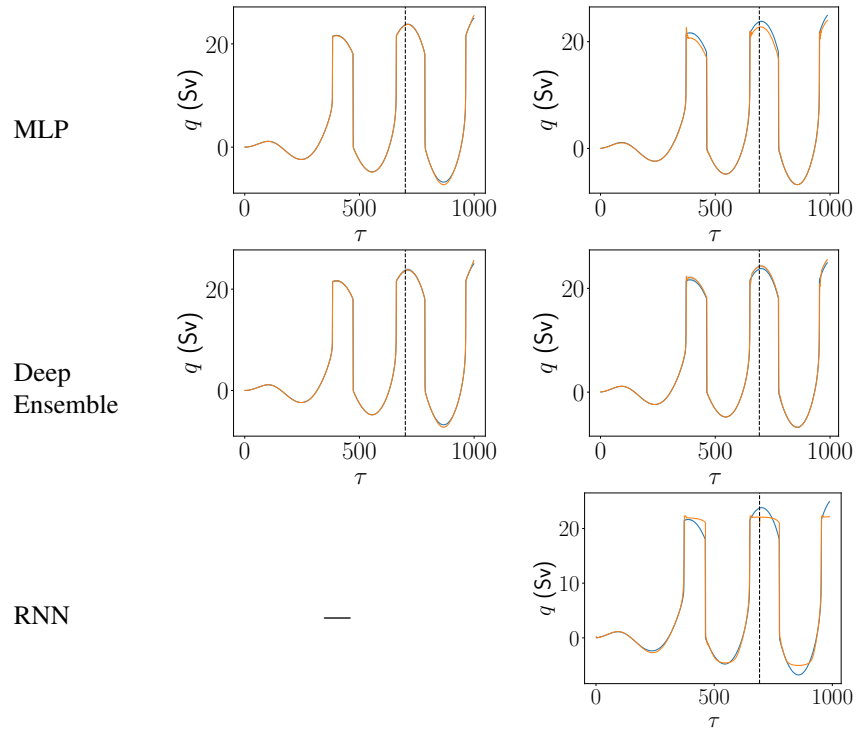
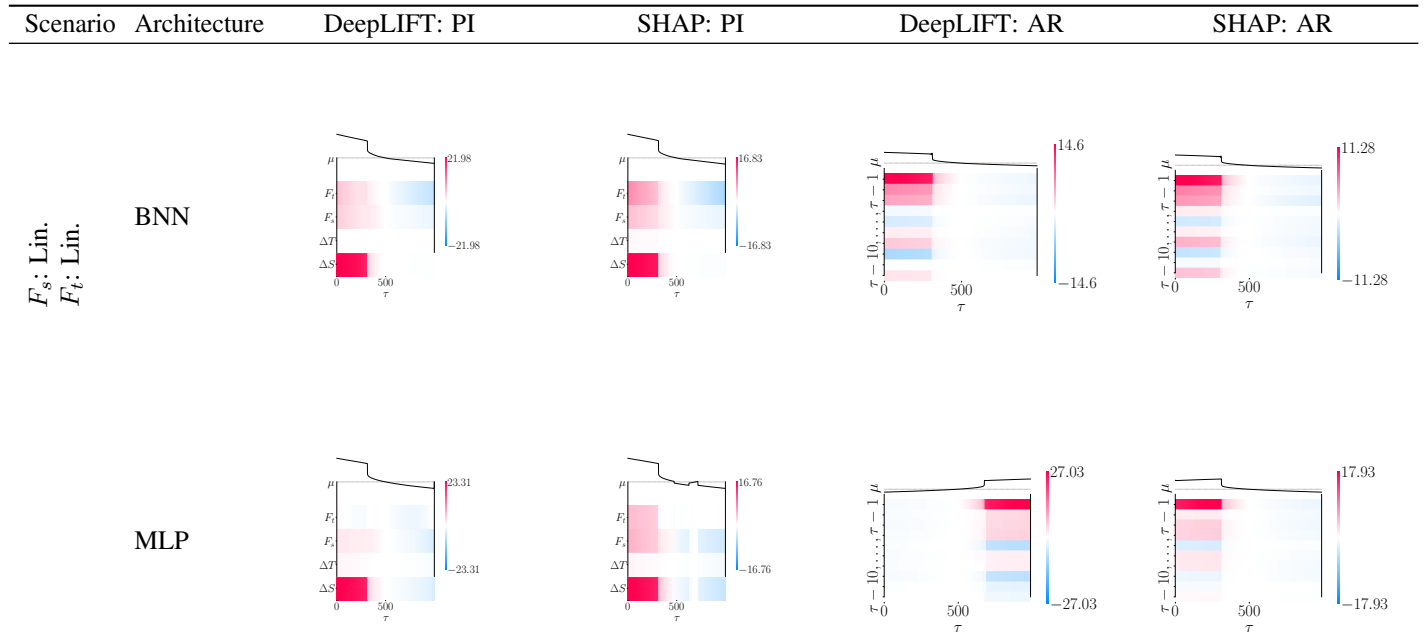


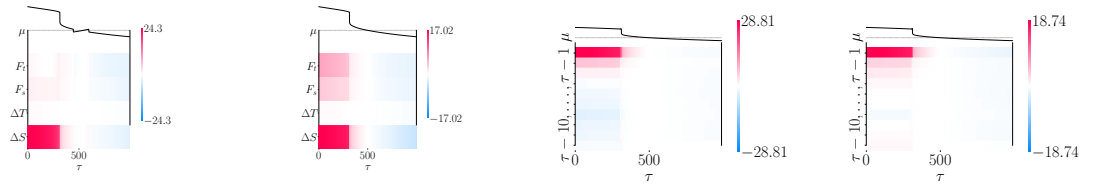
Table 3: Predictive performance using  $F_s$ ,  $F_t$  and  $\rho^{\text{lin}}$ .

C.1.2. EXPLAINABILITY

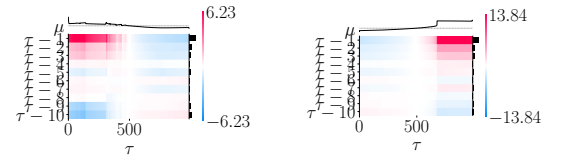


The Importance of Architecture Choice in Deep Learning for Climate Applications

Deep Ensemble

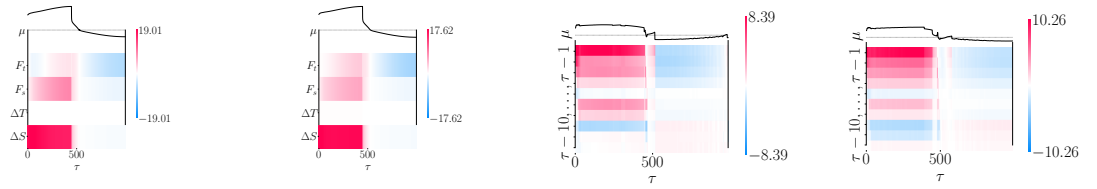


RNN

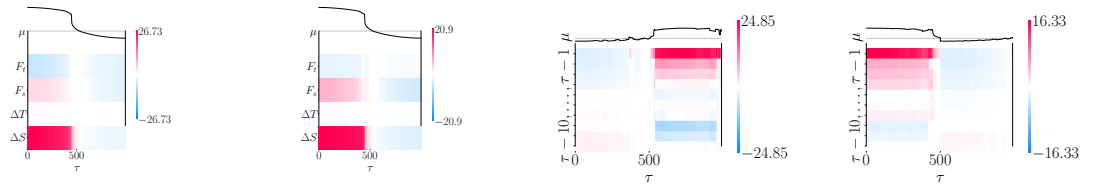


$F_s$ : Sin. (stationary)  
 $F_t$ : Sin. (stationary)

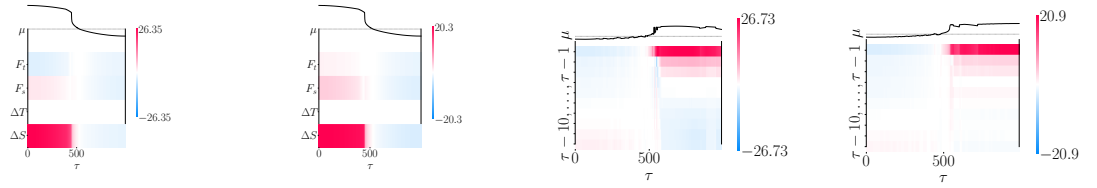
BNN



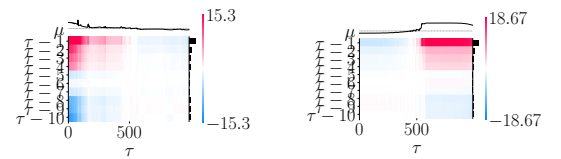
MLP



Deep Ensemble



RNN



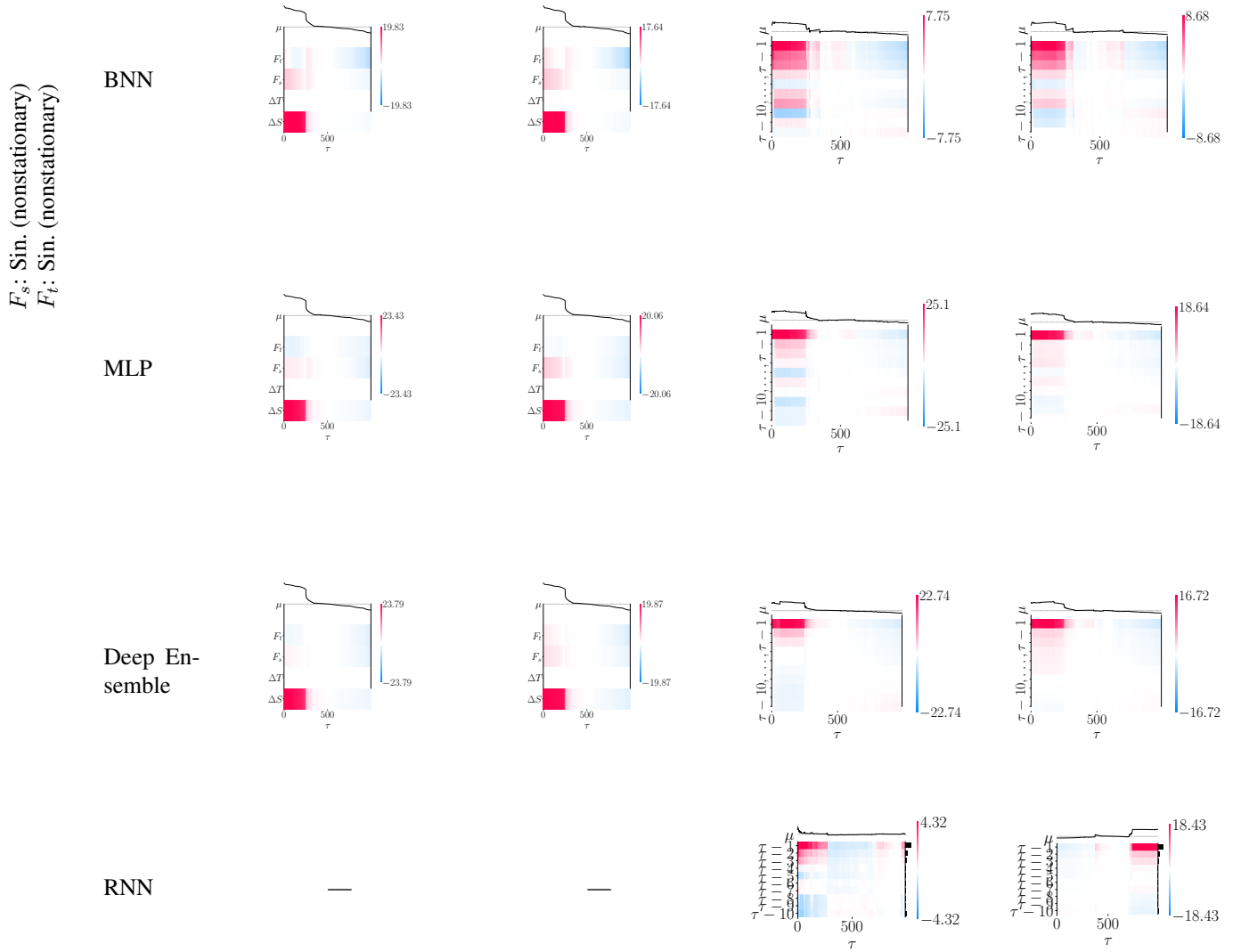


Table 4: Attribution maps using  $F_s$ ,  $F_t$  and  $\rho^{\text{lin}}$ .

## D. $\rho^{\text{EOS-80}}$

In this Appendix, we include supplementary forcing scenarios using  $\rho^{\text{EOS-80}}$  that complement  $\{\mathcal{F}_1, \dots, \mathcal{F}_6\}$  from the main experiments. We include a Recurrent Neural Network (RNN) as an additional architecture.

### D.1. Standard Box Model

#### D.1.1. FORCING SCENARIOS

Scenario	Forcing	Variables	$q$
----------	---------	-----------	-----

The Importance of Architecture Choice in Deep Learning for Climate Applications

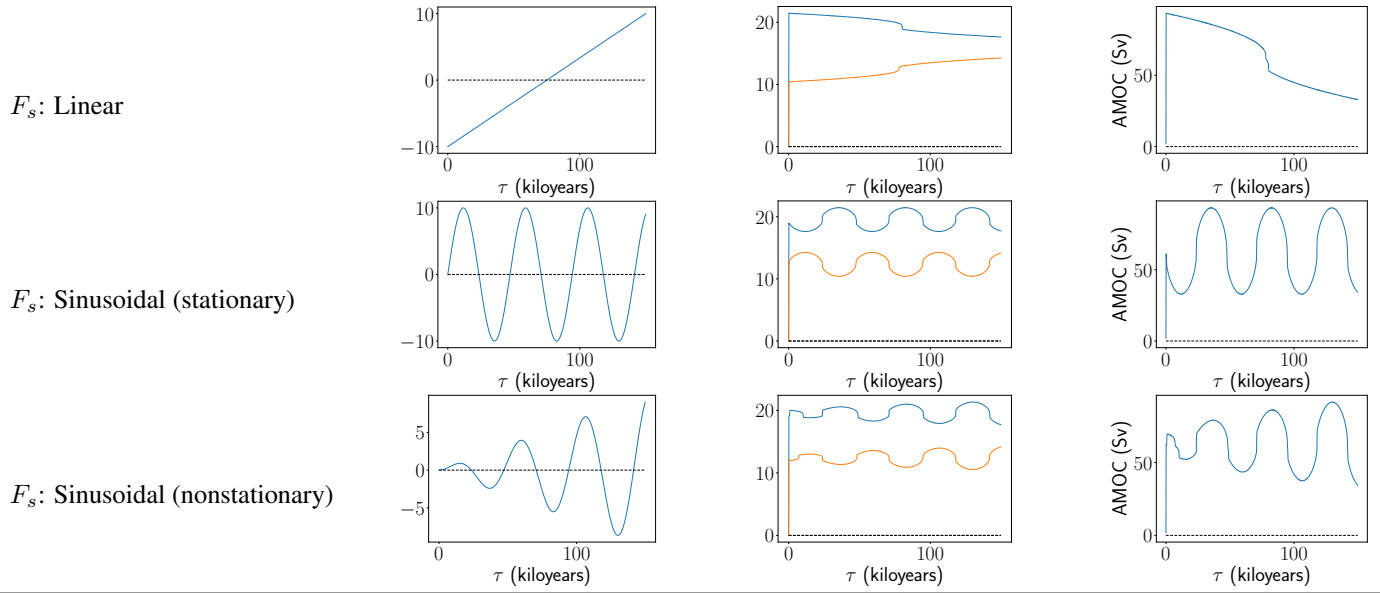
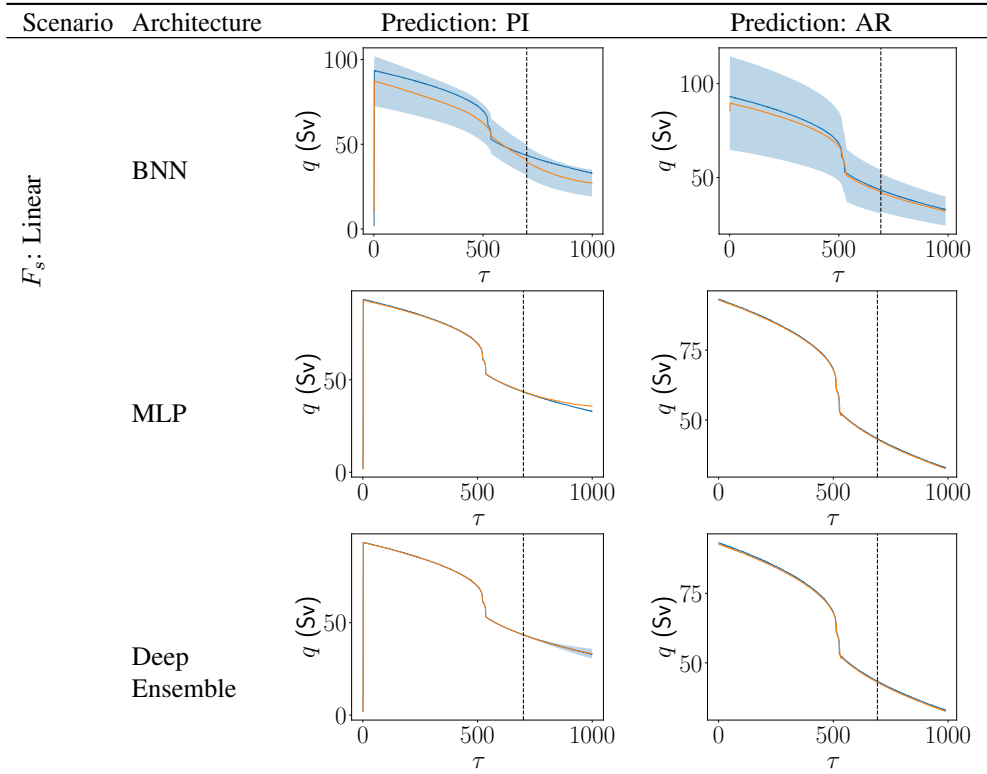
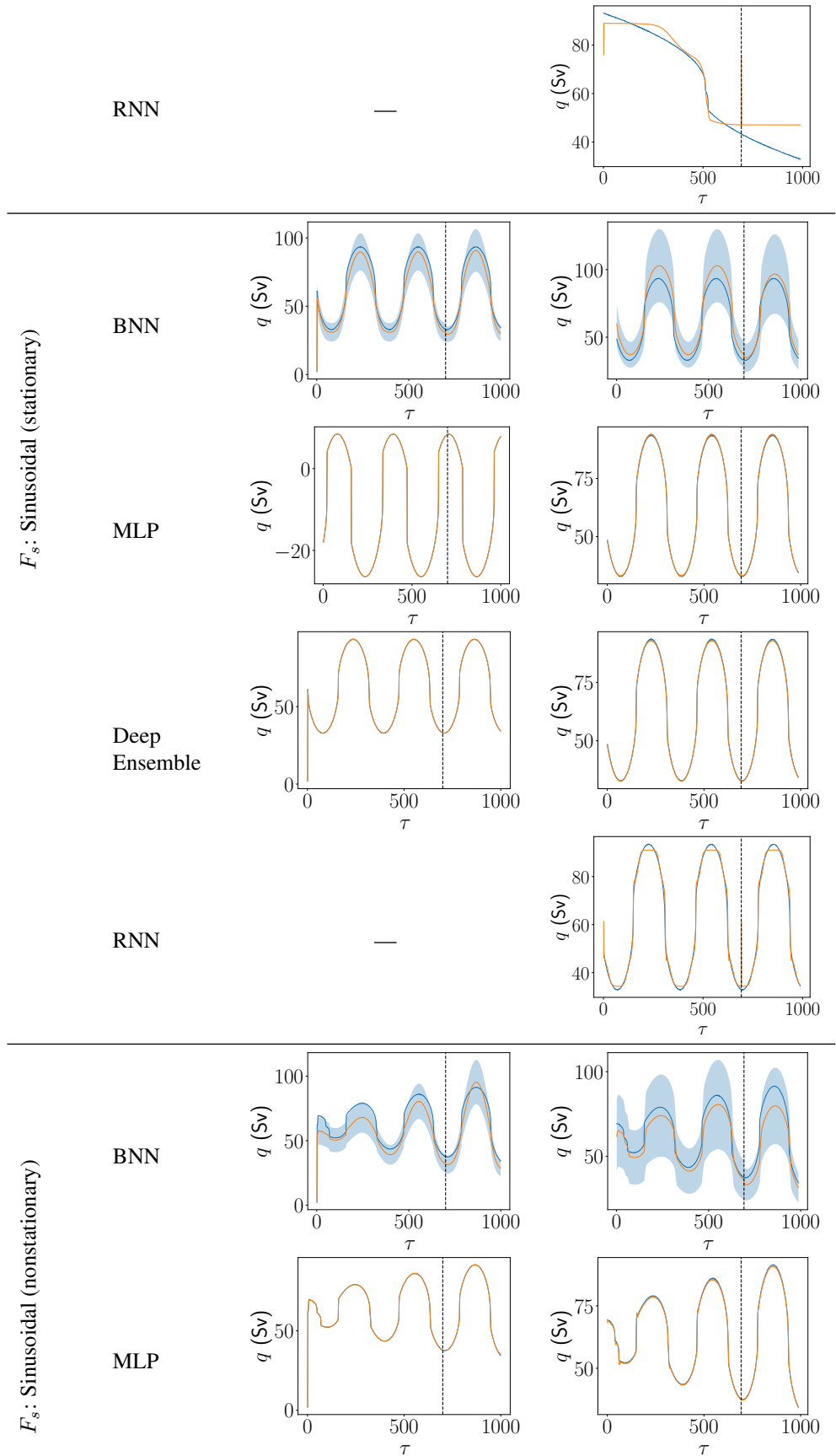


Table 5: Overview of the scenarios and their variables using only fresh water forcing.

D.1.2. PERFORMANCE





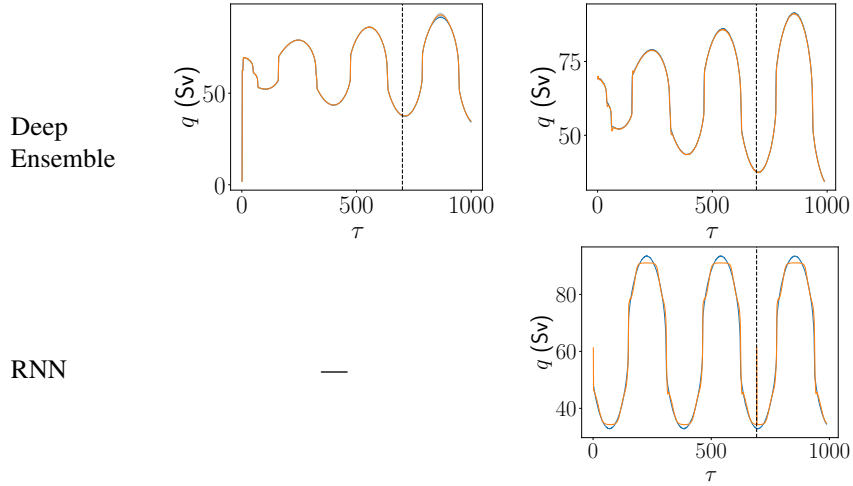
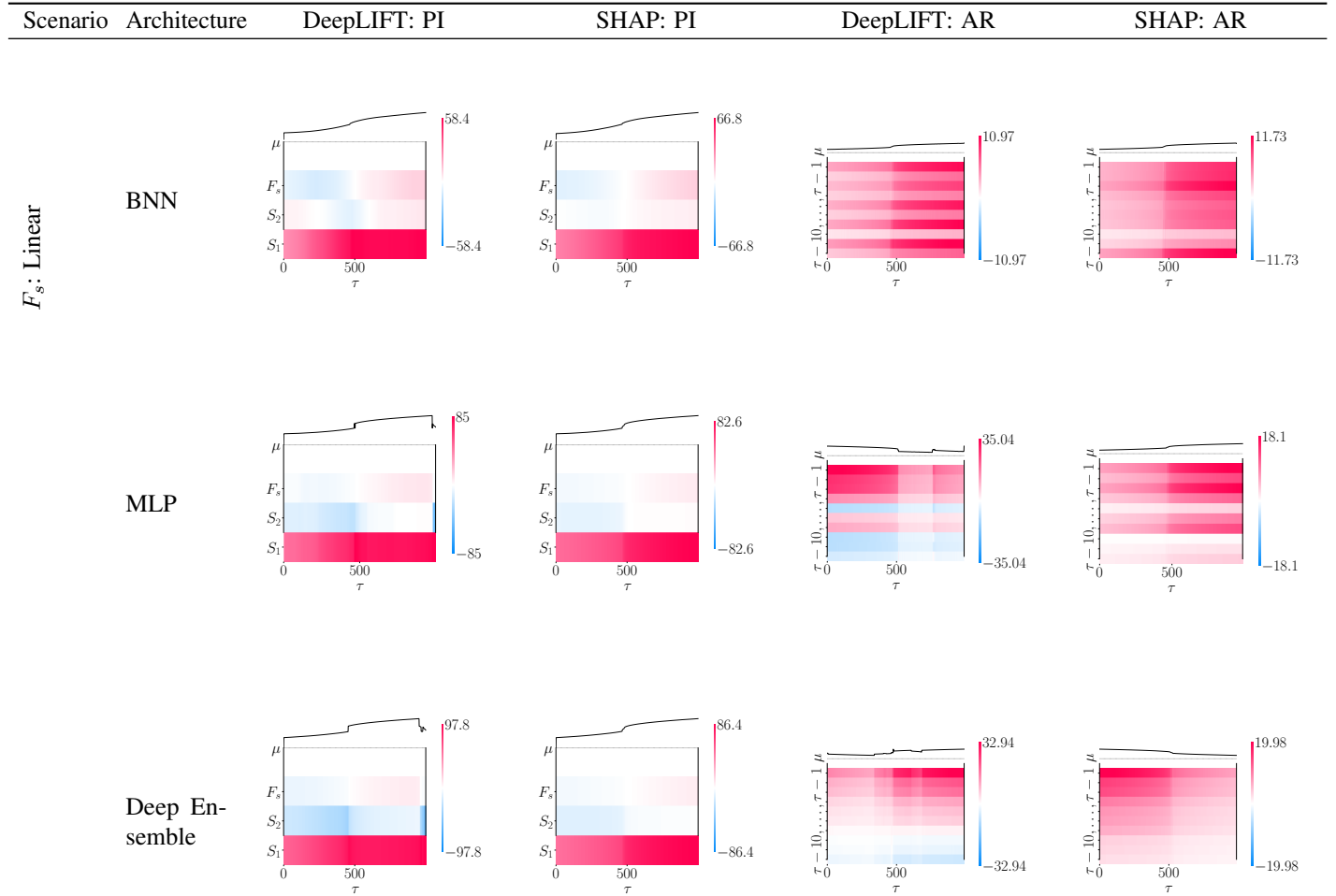


Table 6: Predictive performance using  $F_s$  and  $\rho^{\text{EOS-80}}$ .

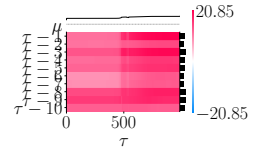
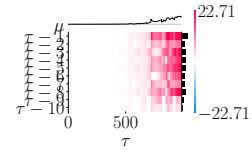
D.1.3. EXPLAINABILITY



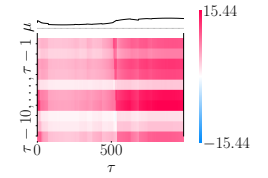
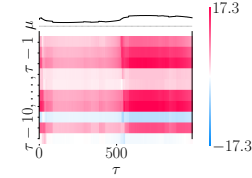
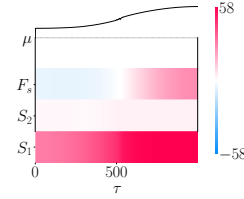
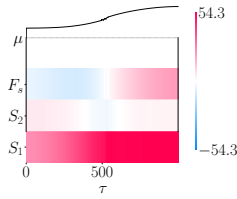
The Importance of Architecture Choice in Deep Learning for Climate Applications

$F_s$ : Sinusoidal (stationary)

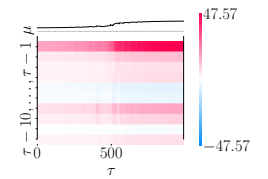
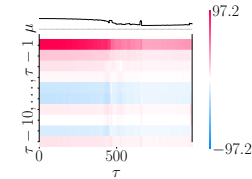
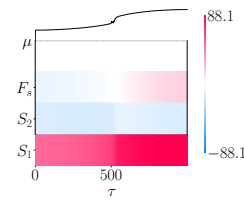
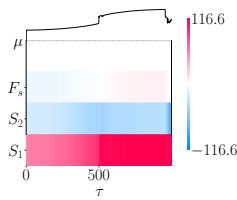
RNN



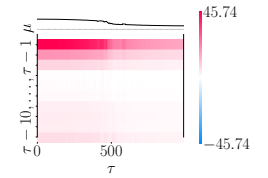
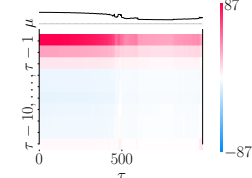
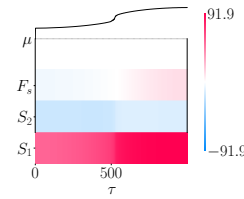
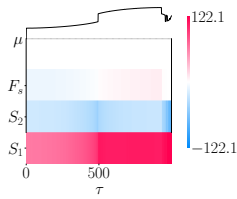
BNN



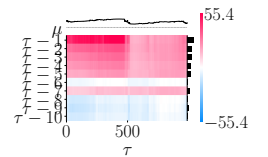
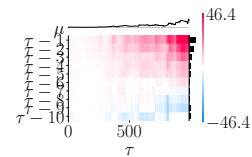
MLP



Deep Ensemble

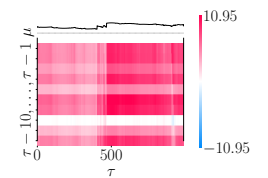
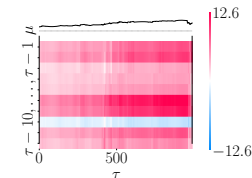
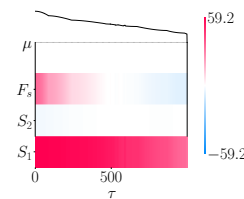
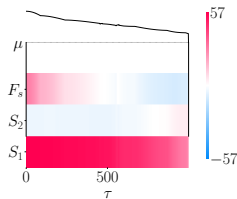


RNN



$F_s$ : Sinusoidal (nonstationary)

BNN



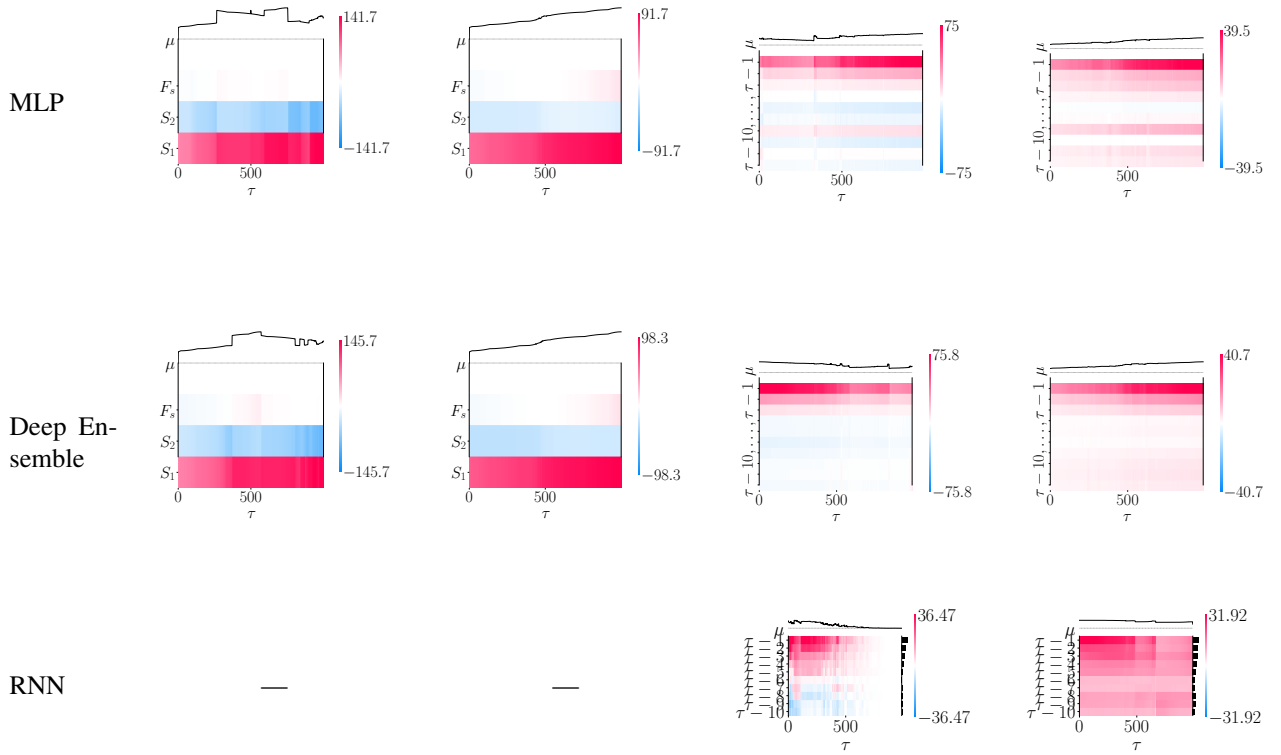


Table 7: Attribution maps using  $F_s$  and  $\rho^{\text{EOS-80}}$ .

### E. BNN Prior Standard Deviation

We conduct additional experiments using the BNN architecture and varying values of the prior standard deviation  $\sigma$ . We set  $\sigma = 1^{-2}, 1^{-3}, 1^{-4}, 1^{-5}, 1^{-6}$ . Note that the value in the main experiments was  $\sigma = 0.1$ .

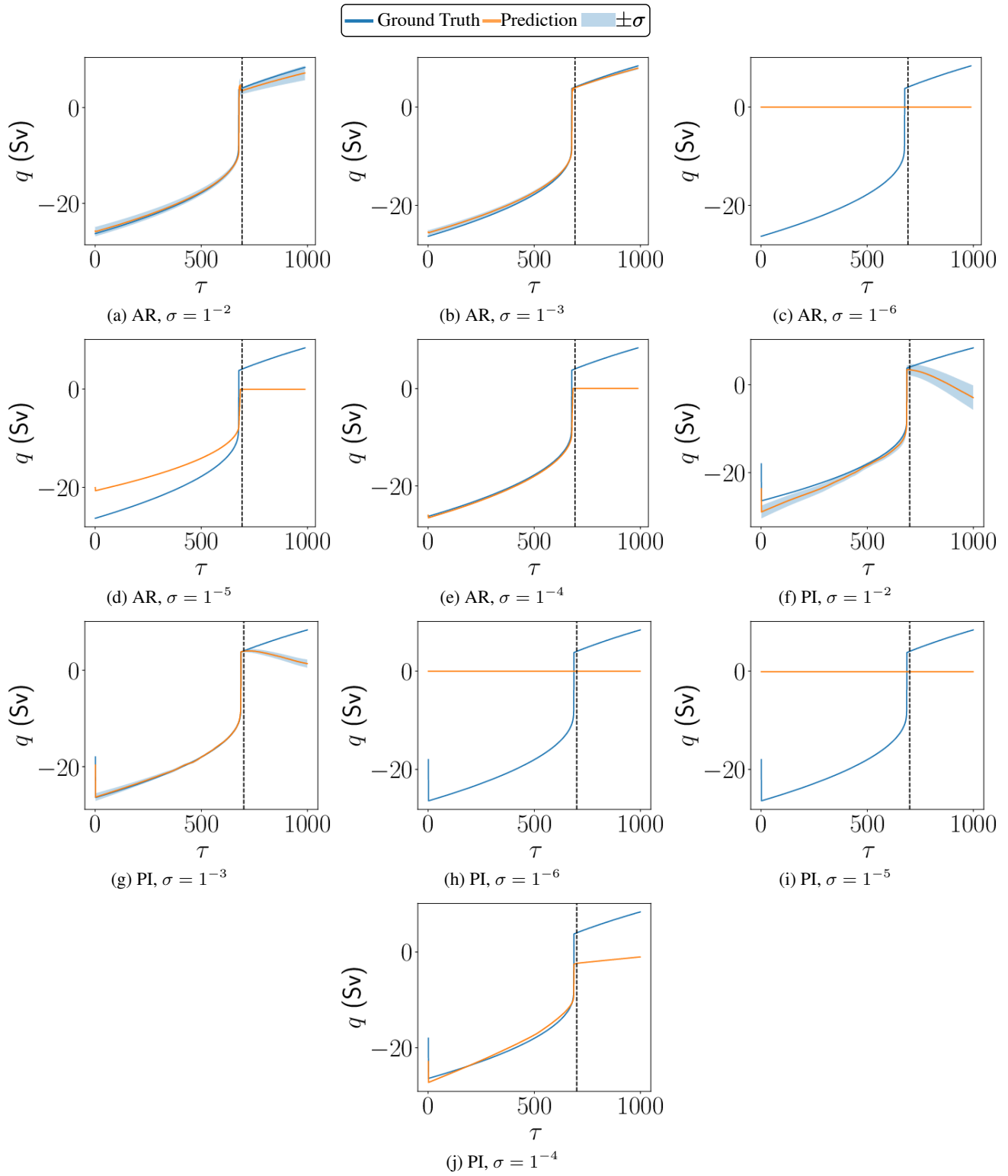


Figure 27. BNN predictions under varying  $\sigma$  for  $\mathcal{F}_1$ .

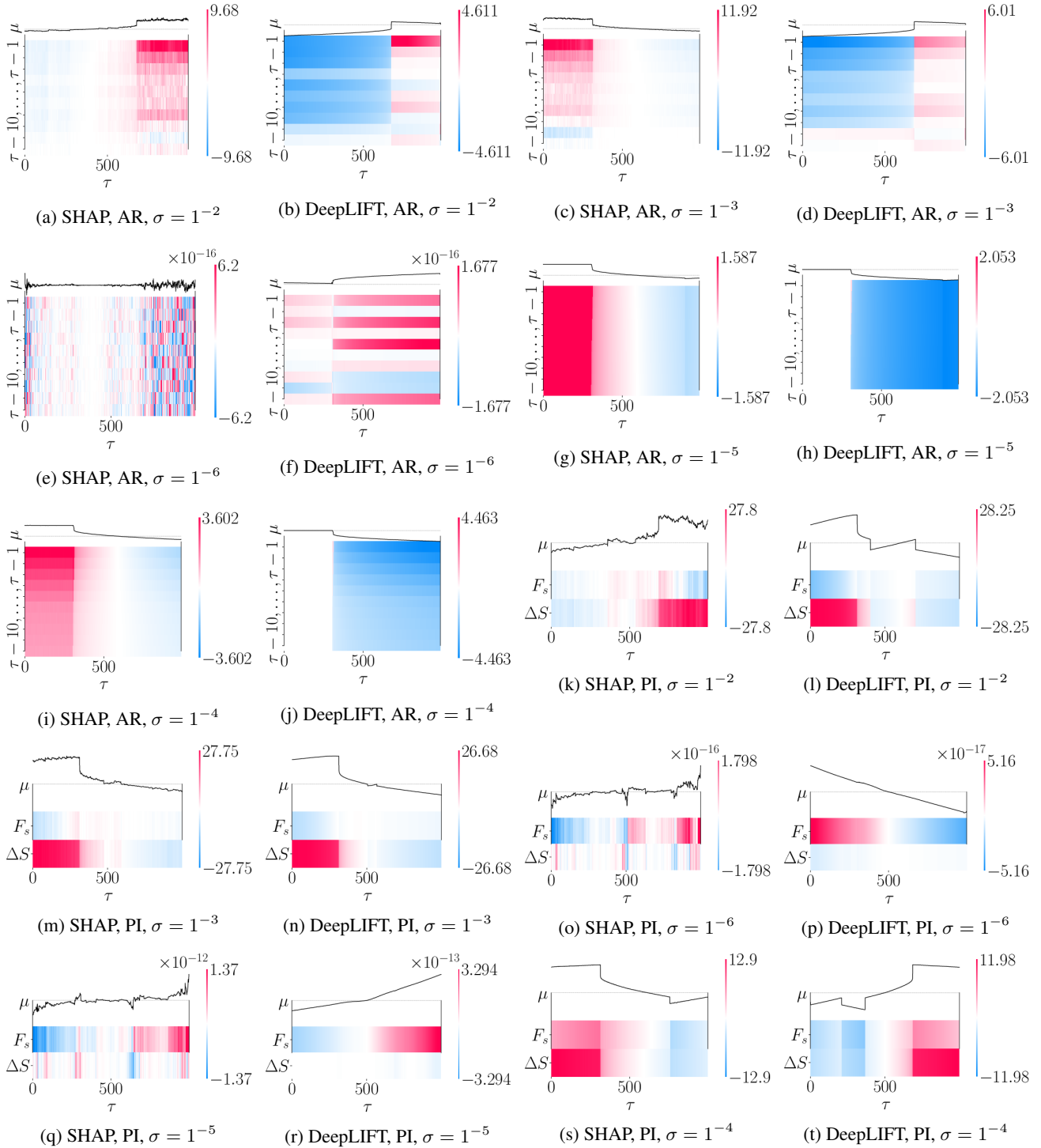


Figure 28. BNN attributions under varying  $\sigma$  for  $\mathcal{F}_1$ .

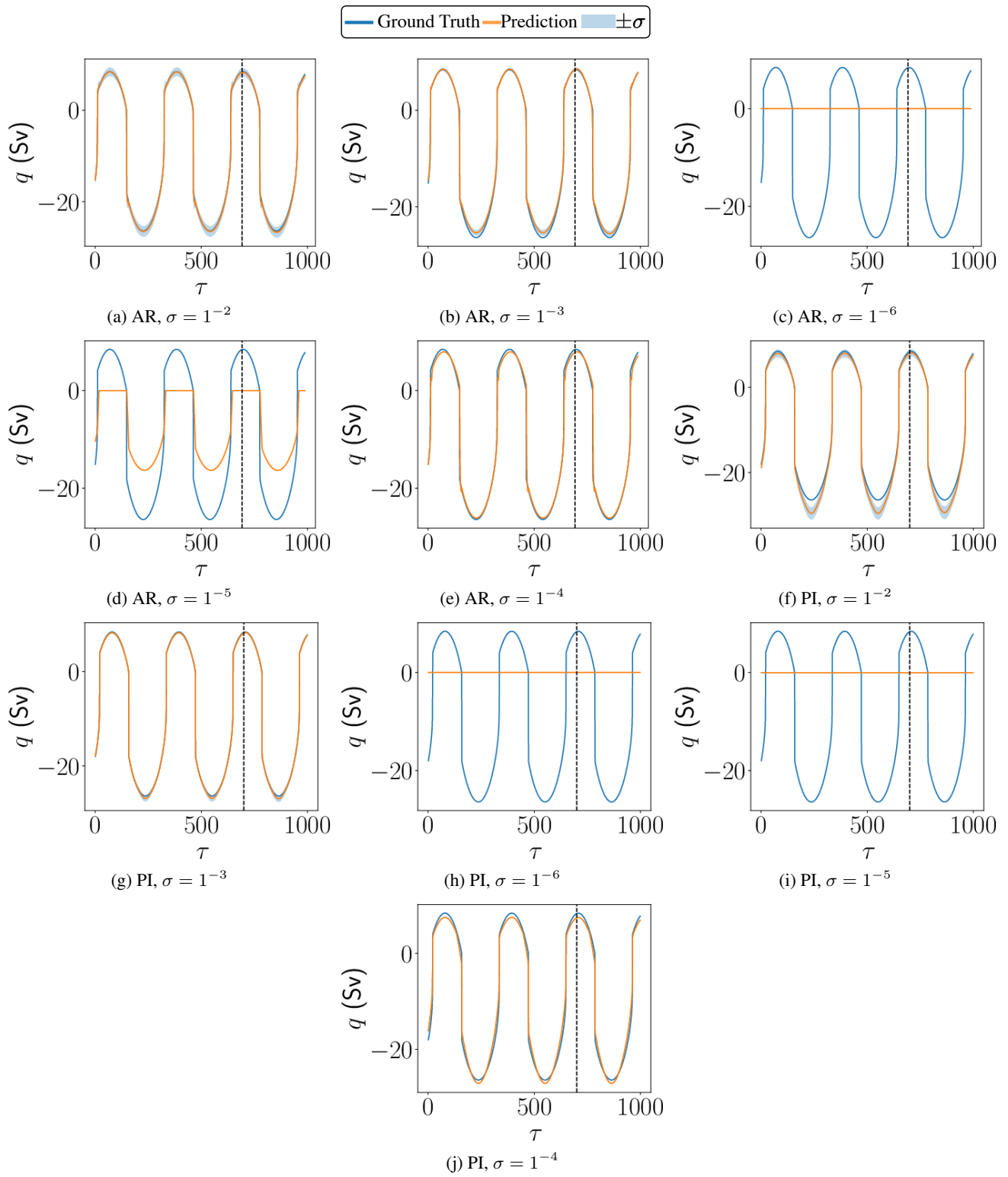


Figure 29. BNN predictions under varying  $\sigma$  for  $\mathcal{F}_2$ .

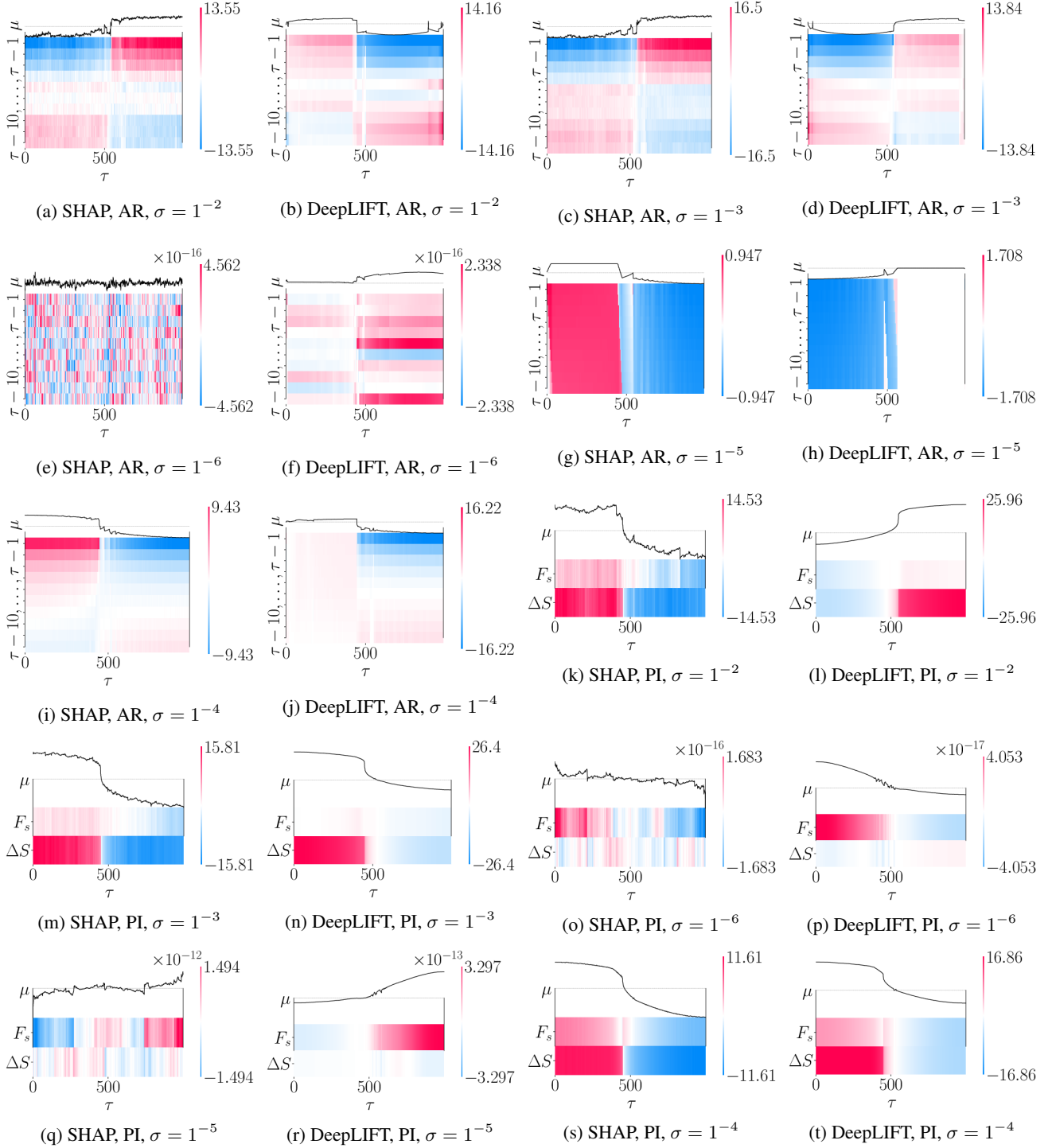


Figure 30. BNN attributions under varying  $\sigma$  for  $\mathcal{F}_2$ .

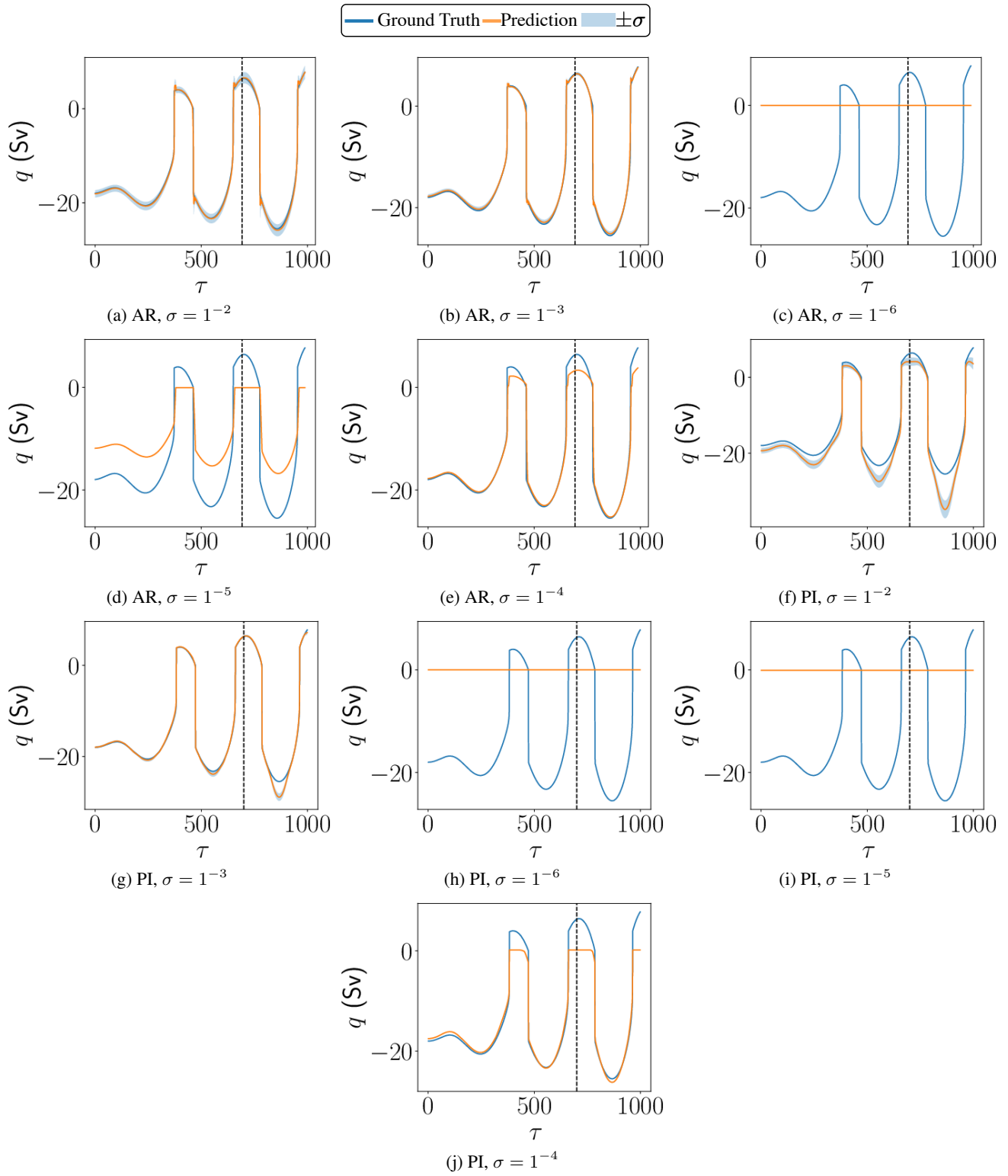


Figure 31. BNN predictions under varying  $\sigma$  for  $\mathcal{F}_3$ .

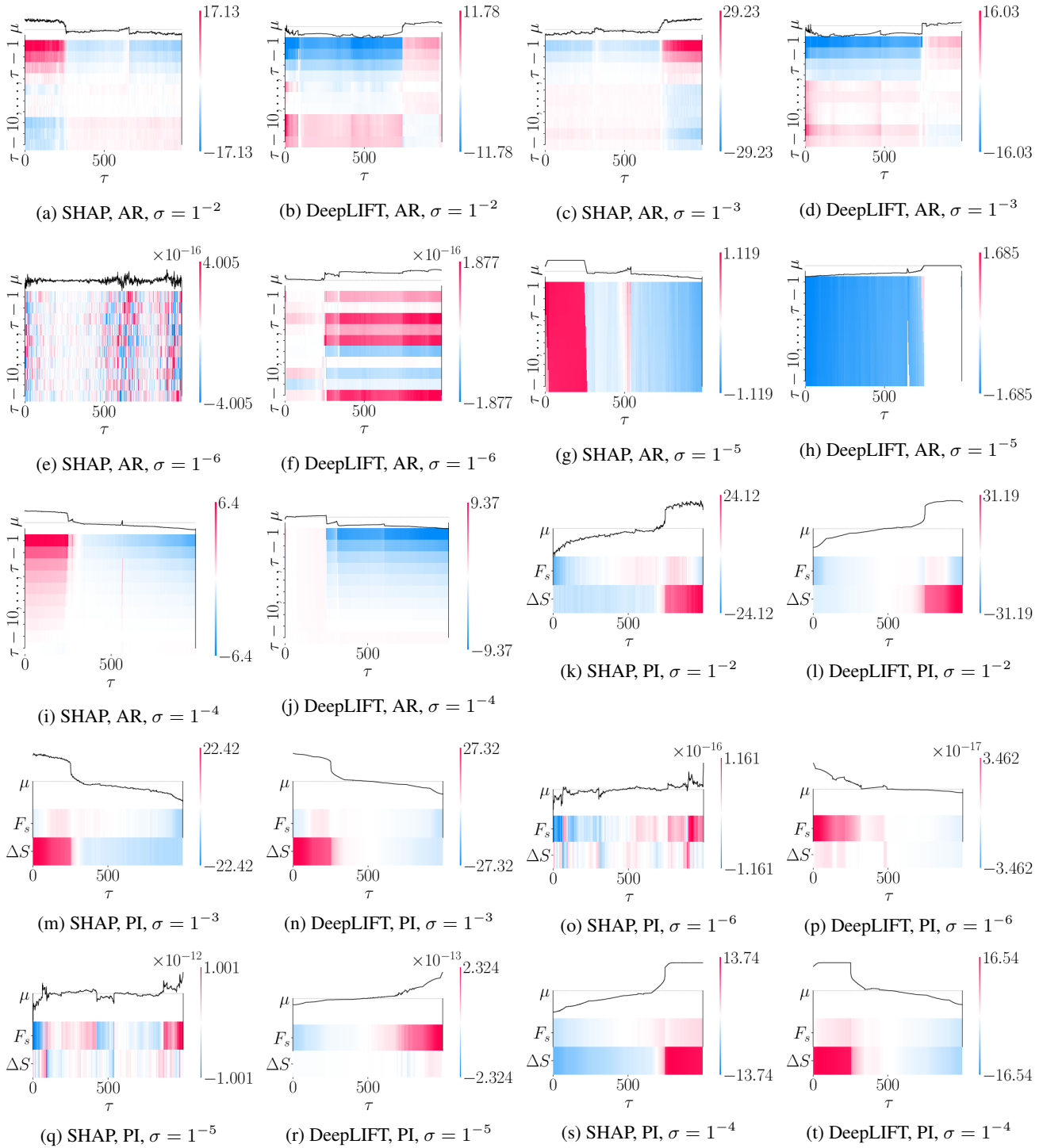


Figure 32. BNN attributions under varying  $\sigma$  for  $\mathcal{F}_3$ .

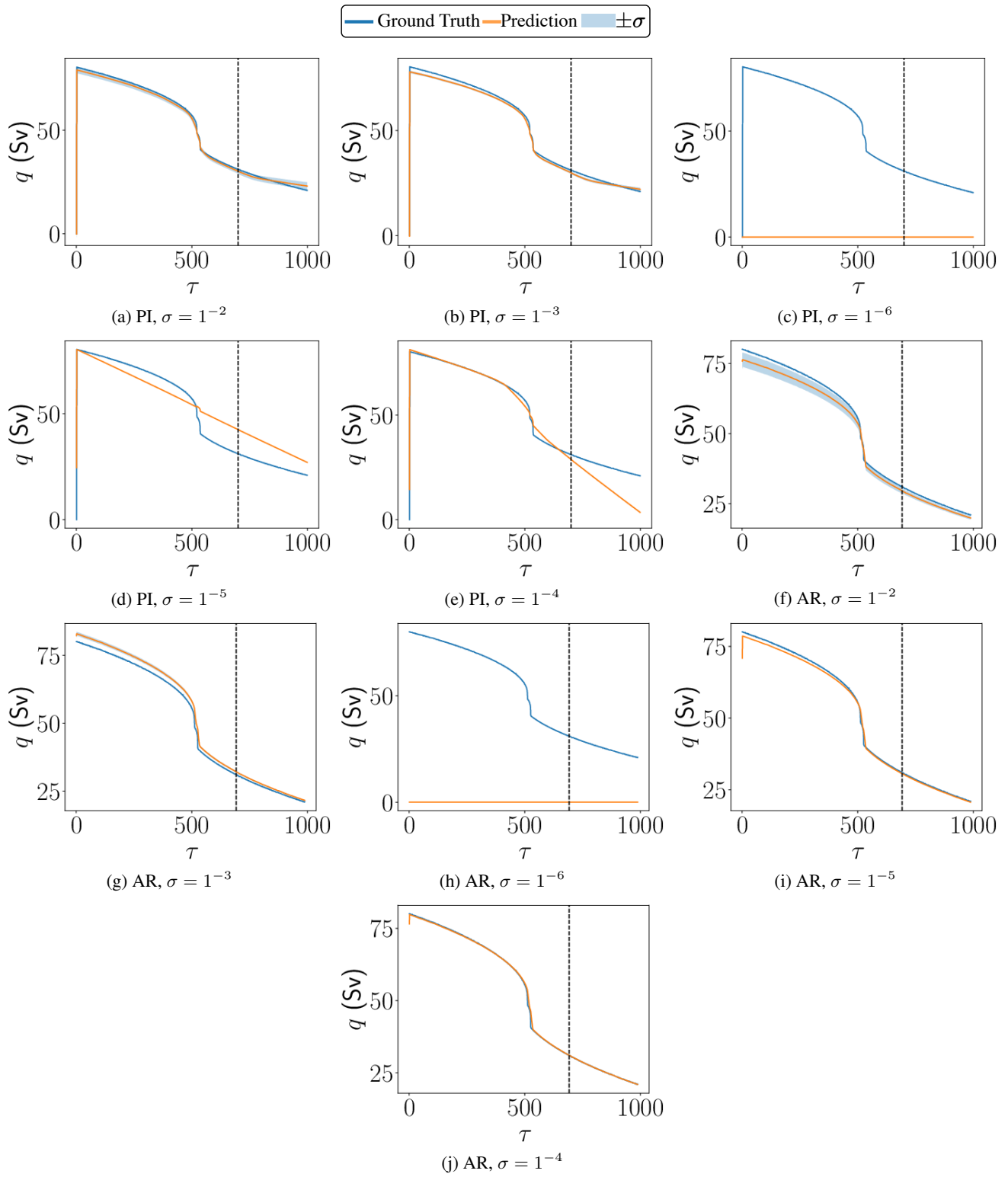


Figure 33. BNN predictions under varying  $\sigma$  for  $\mathcal{F}_4$ .

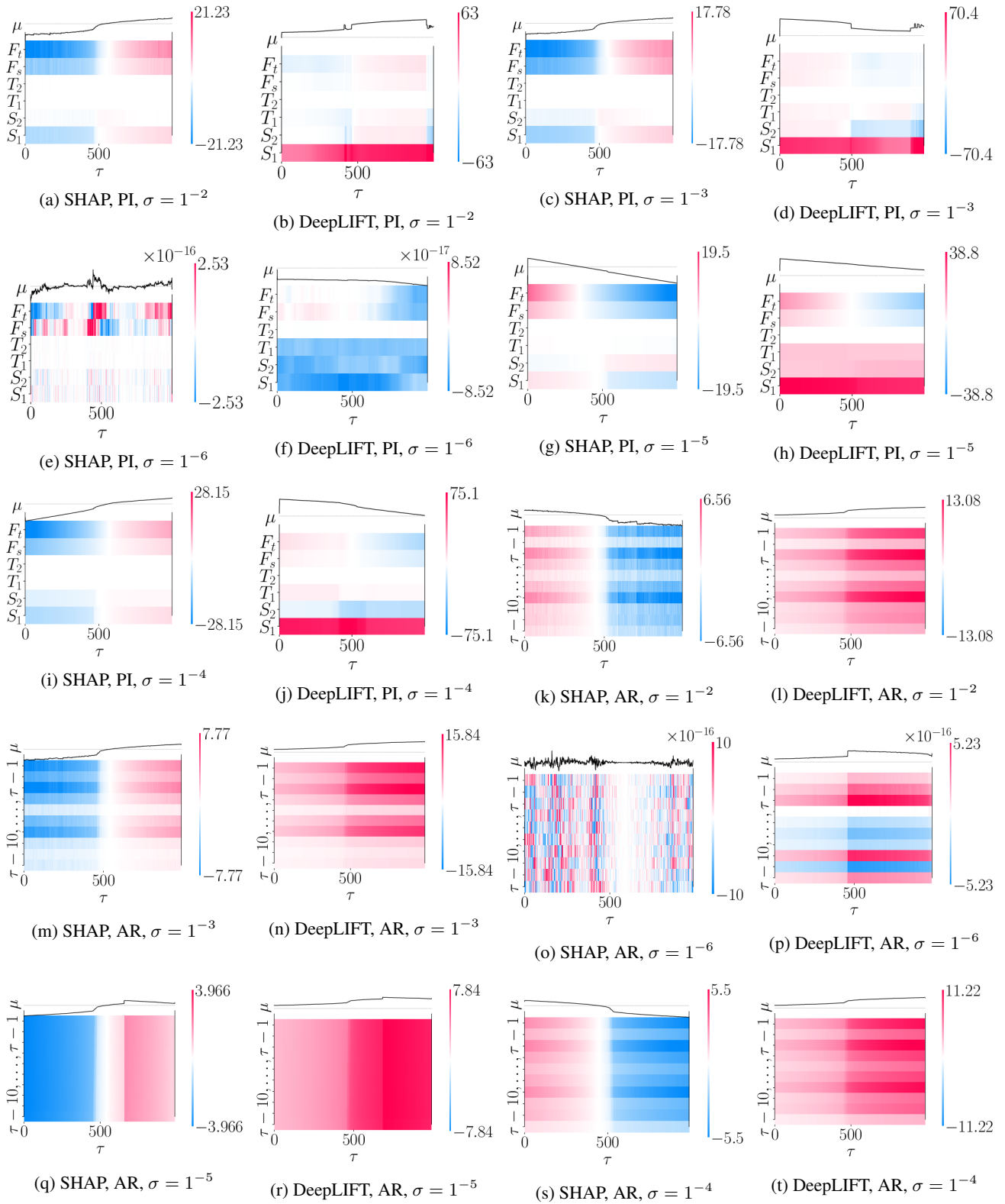


Figure 34. BNN attributions under varying  $\sigma$  for  $\mathcal{F}_4$ .

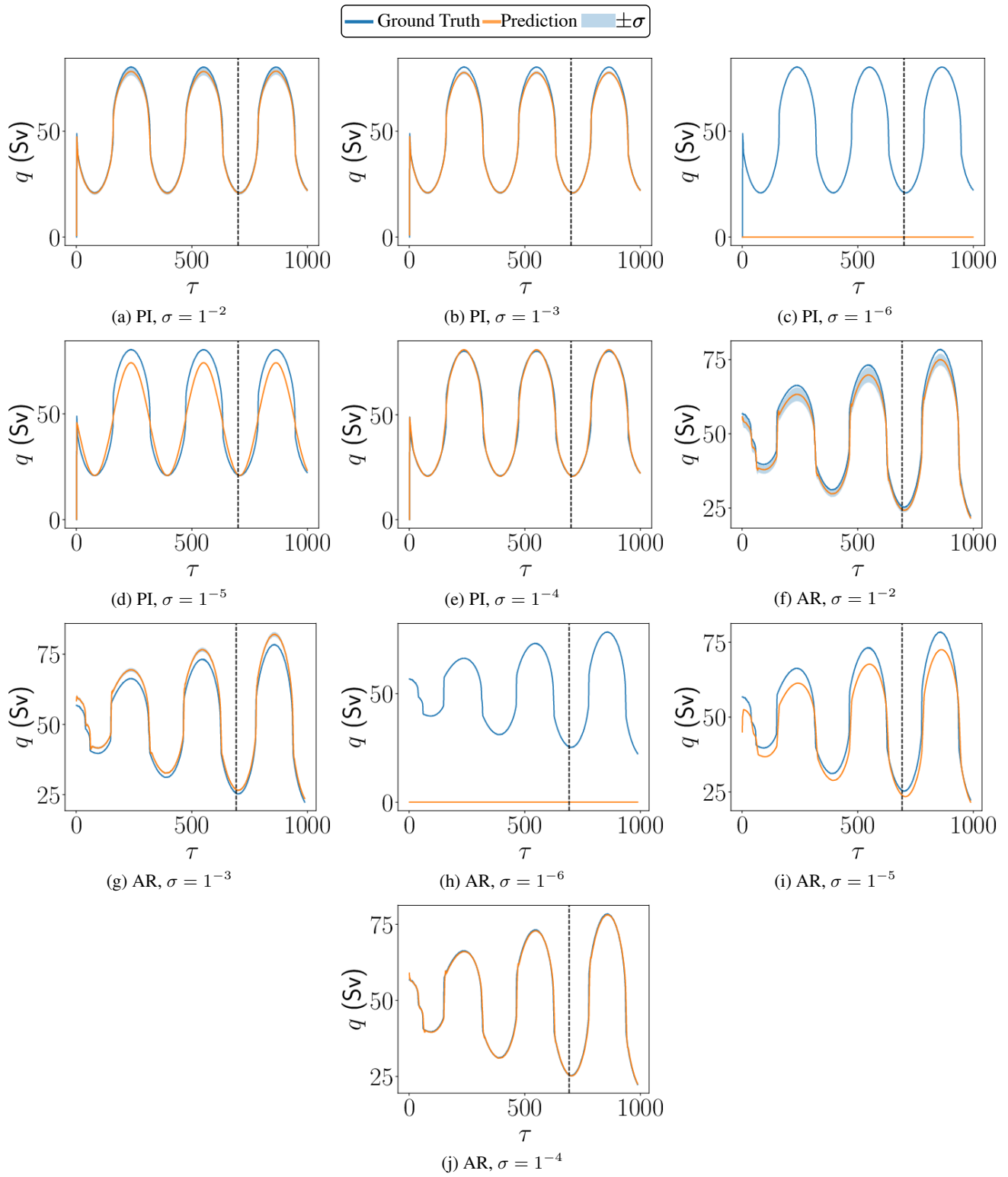


Figure 35. BNN predictions under varying  $\sigma$  for  $\mathcal{F}_5$ .

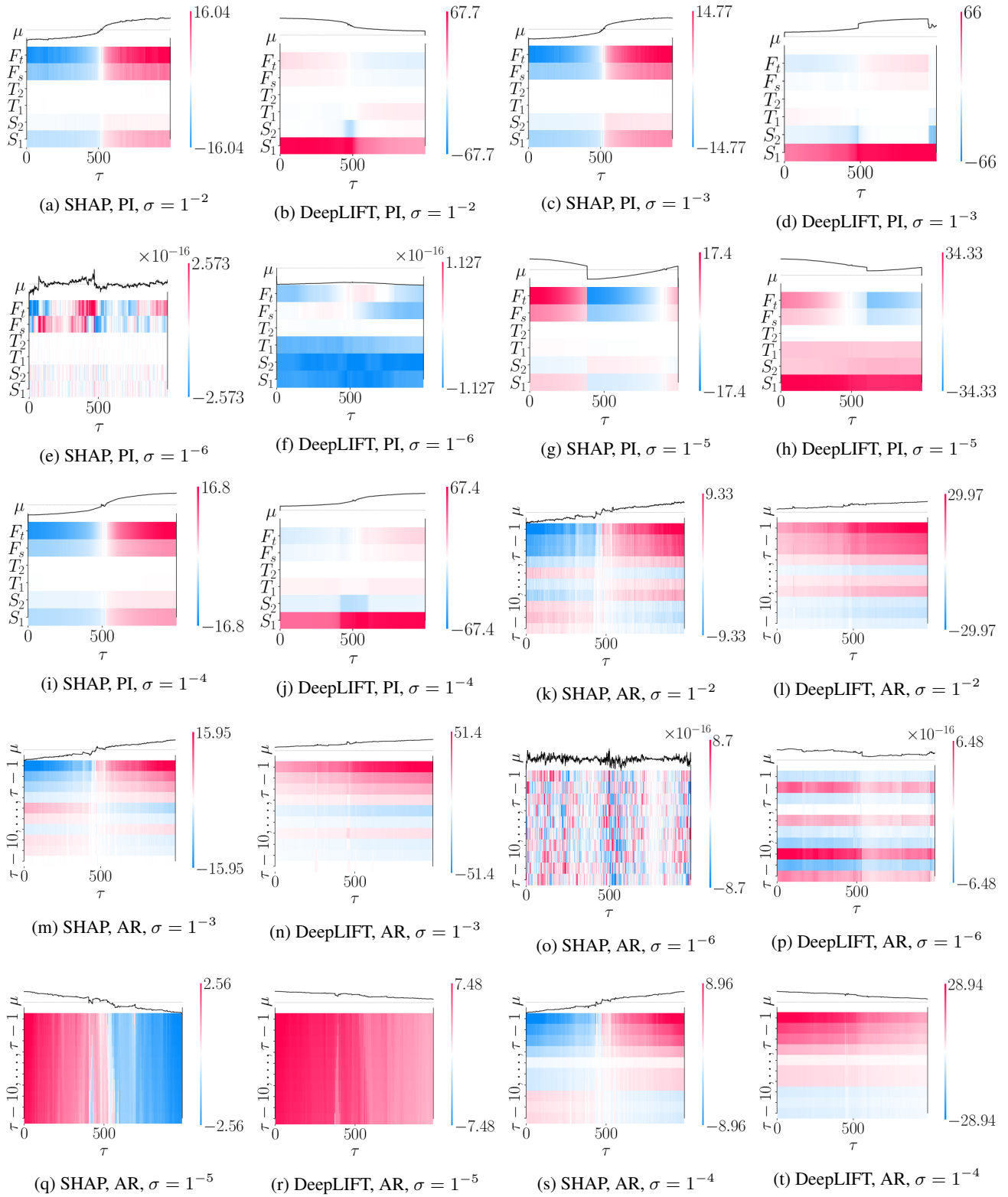


Figure 36. BNN attributions under varying  $\sigma$  for  $\mathcal{F}_5$ .

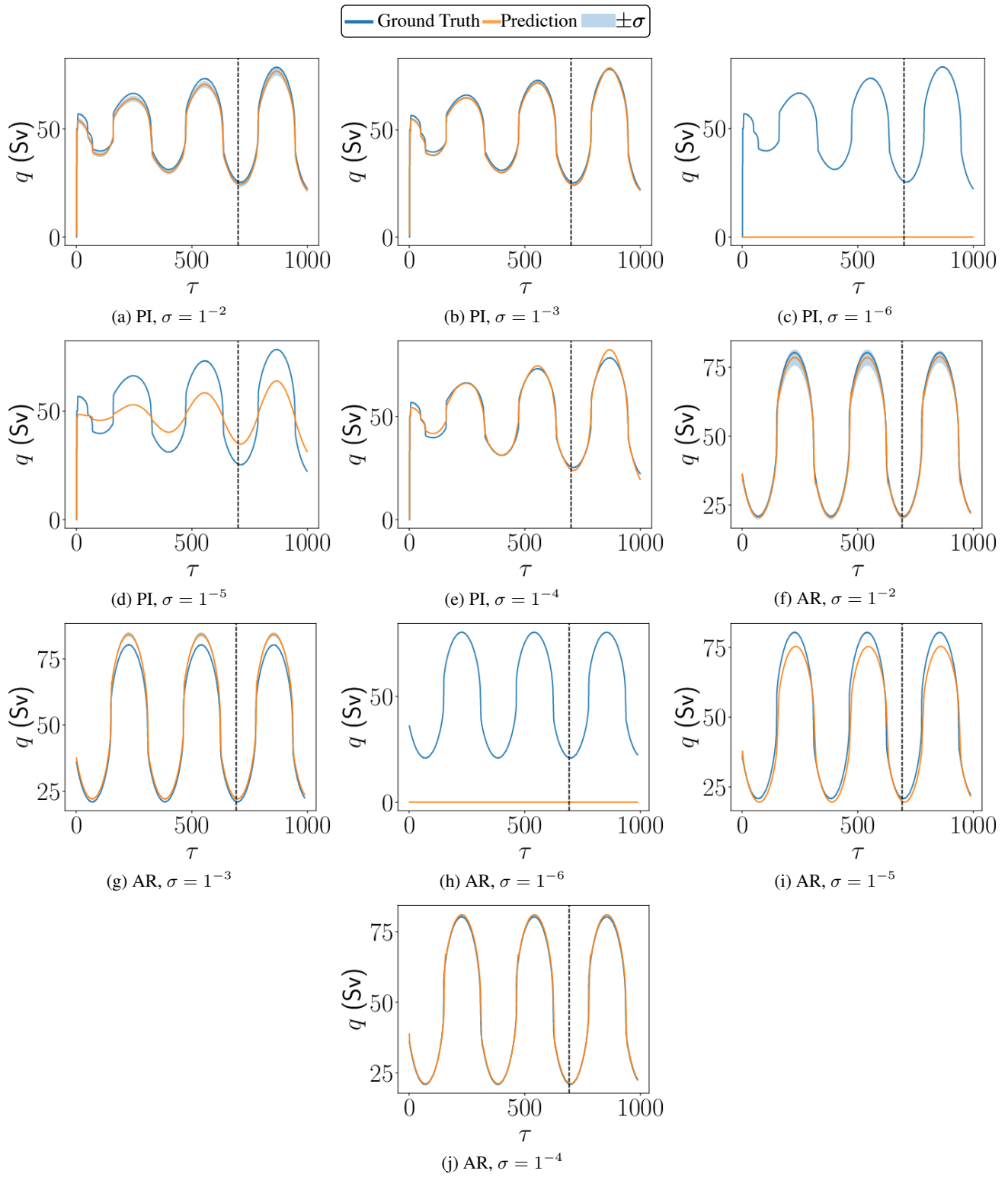


Figure 37. BNN predictions under varying  $\sigma$  for  $\mathcal{F}_6$ .

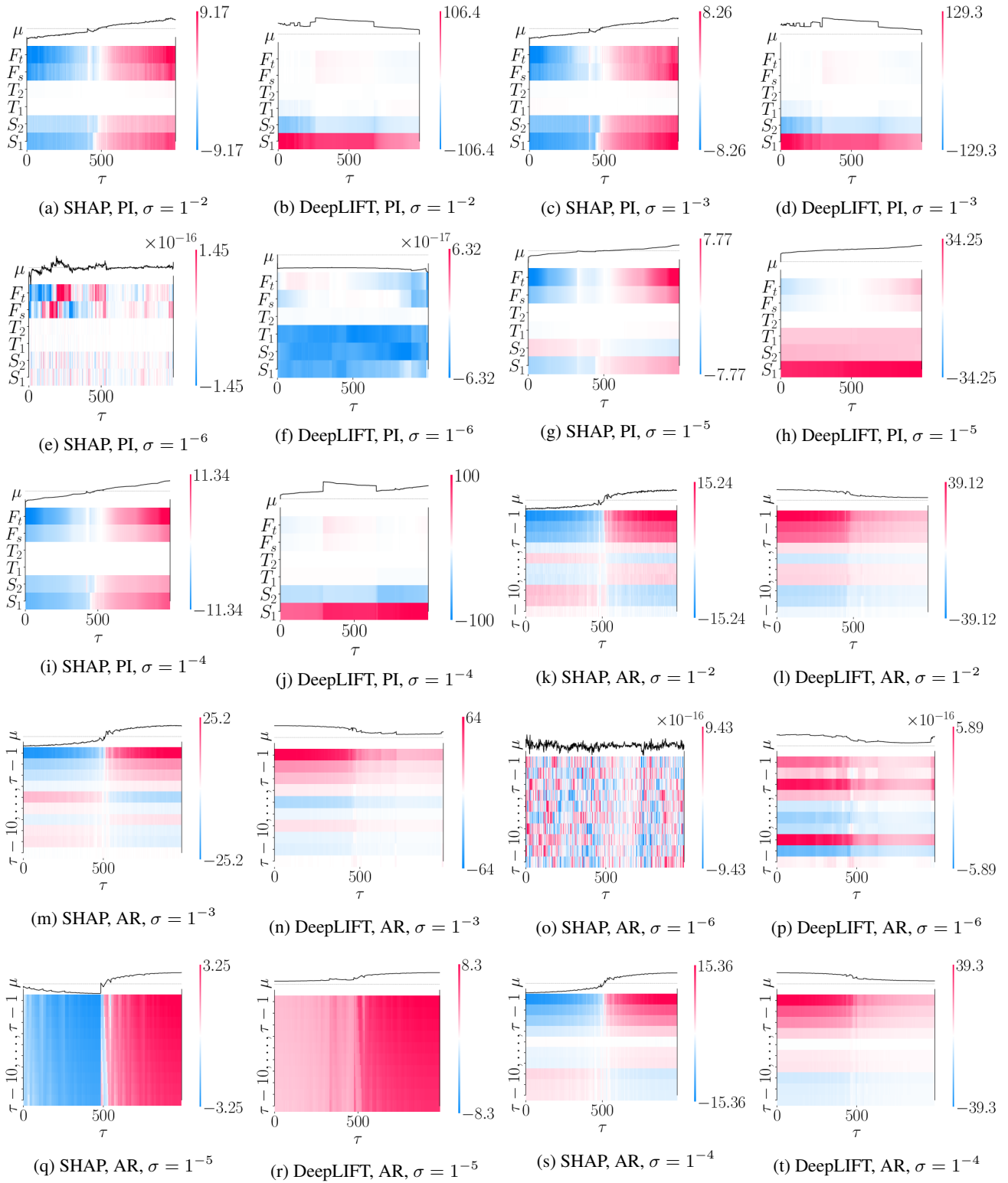


Figure 38. BNN attributions under varying  $\sigma$  for  $\mathcal{F}_6$ .